Integrating multimodal, multiscale connectivity blueprints of the cerebral cortex

Justine Y. Hansen[1], Golia Shafiei[2], Katharina Voigt[3,4], Emma X. Liang[4],

Sylvia M. L. Cox[5], Marco Leyton[1,5], Sharna D. Jamadar[3,4], Bratislav Misic[1]*

[1]*Montréal Neurological Institute, McGill University, Montréal, QC, Canada*
[2]*Department of Psychiatry, Perelman School of Medicine,*
University of Pennsylvania, Philadelphia, PA 19104, USA
[3]*School of Psychological Sciences Turner and Turner Institute for Brain and Mental Health,*
Monash University, 18 Innovation Walk, 3800 Clayton VIC, Australia.
[4]*Monash Biomedical Imaging, Monash University, 770 Blackburn Road, 3800 Clayton VIC, Australia.*
[5]*Department of Psychiatry, McGill University, Montréal, QC, Canada*

The brain is composed of disparate neural populations that communicate and interact with one another. Although fiber bundles, similarities in molecular architecture, and synchronized neural activity all reflect how brain regions potentially interact with one another, a comprehensive study of how all these inter-regional relationships jointly reflect brain structure and function remains missing. Here we systematically integrate seven multimodal, multiscale types of inter-regional similarity ("connectivity modes") derived from gene expression, neurotransmitter receptor density, cellular morphology, glucose metabolism, haemodynamic activity, and electrophysiology. We uncover a compact set of universal organizational principles whereby all types of inter-regional relationships reflect brain geometry and anatomical connectivity. Connectivity modes also exhibit unique and diverse connection patterns, hub profiles, spatial gradients, and modular organization. Throughout, we observe a consistent primacy of molecular connectivity modes—namely correlated gene expression and receptor similarity—that map onto multiple phenomena, including the rich club and patterns of cortical abnormalities across 13 neurological, psychiatric, and neurodevelopmental disorders. Finally, to construct a single multimodal wiring map of the brain, we fuse all seven connectivity modes and show that the fused network maps onto major organizational features of the brain including structural connectivity, intrinsic functional networks, and cytoarchitectonic classes. Altogether, this work sets the stage for next-generation connectomics and the integrative study of inter-regional relationships.

INTRODUCTION

Brain connectivity classically refers to the physical neural fibers that link disparate neuronal populations. Axonal projections can be reconstructed by imaging fluorescently-labelled proteins that are either injected into or genetically expressed by a cell, or by stacking electron microscopy images of thinly sliced brain sections [84, 89]. At the macroscale, diffusion-weighted imaging can be used to trace large fiber bundles that connect pairs of brain regions *in vivo*, which collectively constitute the structural connectome [58, 145]. Across organisms, spatial scales, and imaging techniques, the brain's structural architecture exhibits hallmark features including a prevalence of short range connections resulting in functionally segregated modules [143], and a small number of disproportionately densely interconnected hubs [157]. Ultimately, studying the brain's structural connectome has advanced our understanding of how information is transmitted [8, 133], how brain structure supports function [147], and how perturbations may result in network-defined pathology spread [175].

However, the structural network does not account for the molecular and physiological heterogeneity that exist in the brain. An emerging representation of connectivity is feature similarity: if two brain regions ex-

hibit similar biological features, we might expect them to be related to one another and engaged in common function. As a result, different types of feature similarity are sometimes referred to as "connectivity" despite the fact that they don't represent direct axonal connections [1]. This approach is already widely used on the BOLD signal where haemodynamic time courses are correlated with each other, and also exists for time-series measures from other imaging modalities such as magneto-/electroencephalography (MEG/EEG) and dynamic FDG-fPET (all called "functional connectivity") [25, 33, 49, 55, 75]. In cases where multiple measures of a feature exist at each brain region, such as gene expression levels across many genes, inter-regional similarity can be estimated with respect to a single local feature [60, 61, 65, 112, 120, 131, 134]. In each case, the ensuing region × region correlation matrix represents a form of connectivity between brain regions.

As multiple estimates of inter-regional similarity become available through emerging technologies and data sharing efforts, it becomes possible to integrate them into a single framework and deduce how they interact with one another, and in what ways they are unique or complementary. For example, brain structure is heterogeneously coupled to haemodynamic functional connectivity along the sensory-association cortical hierarchy [14, 163]. Information about inter-regional feature similarity adds additional insight on how structure supports function, and has been shown to improve the structure-function concordance [60, 100, 114]. The advance in

* bratislav.misic@mcgill.ca

neuroimaging techniques and data sharing standards has now made it possible to study multiple forms of inter-regional relationships jointly, spanning a range of spatial and temporal scales. The future of connectomics is therefore no longer limited to structural connectivity, but can be approached from a multi-modal, multi-scale angle.

Here we integrate seven layers of inter-regional relationships, including gene expression, receptor density, cellular composition, metabolism, electrophysiology, and temporal fingerprints, to assemble a comprehensive, multiscale wiring blueprint of the cerebral cortex. Although they are all effectively networks reconstructed by correlating feature similarity, hereafter we refer to them as connectivity modes. First, we establish the common and unique manners in which connectivity modes reflect brain structure and geometry. Next, we identify cross-modal hubs as well as circuits that consistently display large inter-regional similarity across multiple connectivity modes. We then test how different connectivity modes capture patterns of cortical abnormalities across 13 neurological, psychiatric, and neurodevelopmental disorders. Moreover, we show that connectivity modes demonstrate diverse gradient and modular decompositions. Finally, we iteratively fuse all seven connectivity modes into a single multimodal network. All seven connectivity modes are publicly available in three parcellation resolutions (https://github.com/netneurolab/hansen_many_networks), in hopes of facilitating integrative, multi-scale analysis of human brain connectivity.

RESULTS

For each brain feature, a similarity network can be represented as a region $\times$ region matrix. Rows and columns represent brain regions, and elements—the edges of the similarity network—represent how similarly two brain regions present the specific feature. This similarity can also be thought of as connectedness, such that two brain regions that share similar features are considered strongly connected. For simplicity, we therefore refer to correlation-based similarity as "connectivity" and the similarity networks as "connectivity modes". To comprehensively benchmark cortical connectivity modes, we construct and analyze seven different connectivity matrices, spanning multiple spatial and temporal scales. These include: (1) correlated gene expression, describing transcriptional similarity across $> 8\,000$ genes from the Allen Human Brain Atlas [63]; (2) receptor similarity, describing how correlated pairs of brain regions are in terms of protein density of 18 neurotransmitter receptors/transporters [60]; (3) laminar similarity, describing how correlated pairs of brain regions are in terms of cell-staining intensity profiles from the BigBrain atlas [4, 112]; (4) metabolic connectivity, measured as the correlation of dynamic FDG-PET (glucose uptake) time-series [74, 75]; (5) haemodynamic resting-state connectivity, measured as the correlation of fMRI BOLD

time-series from the Human Connectome Project (HCP) [160]; (6) electrophysiological connectivity, measured as the first principal component of resting-state MEG connectivity across six canonical frequency bands from the HCP [135, 160]; and (7) temporal profile similarity, a comprehensive account for dynamic similarity (above and beyond a Pearson's correlation between time-series, as is the case in haemodynaimc connectivity) which is measured as the correlation between time-series features of the fMRI BOLD signal [51, 52, 137]. To facilitate comparison between networks, and to mitigate differences between data types and processing pipelines, each network was parcellated to 400 cortical regions and edge values were normalized using Fisher's r-to-z transform [129]. Networks were also parcellated to an alternative functional and anatomical cortical atlas in multiple resolutions (100 and 68 brain regions) for the sensitivity and replication analyses (see *Sensitivity and replication analysis*).

Common organizational principles of connectivity modes

In Fig. 1a, we visualize each normalized connectivity matrix as a heatmap where the colourbar limits are -3 and 3 standard deviations of the edge weight distribution (for edge weight distributions, see Fig. S1a). Brain regions are ordered by left then right hemisphere. Within each hemisphere, regions are further stratified by their membership in the seven canonical intrinsic functional networks (Schaefer-400 parcellation [129, 172]). Homotopic connections stand out, indicating that homologous brain regions in left and right hemispheres are consistently similar to each other no matter the biological feature (Fig. S1b). Previous work has hypothesized that cortical dynamics in homotopic regions are synchronized due to common brainstem input [92, 154]; our work opens an additional hypothesis that similarities in dynamics may also be related to similar molecular composition.

Visually, each connectivity mode demonstrates non-random network organization, which we explore in subsequent sections. Furthermore, similarity between brain regions decreases as both Euclidean and geodesic distance between brain regions increases (Fig. 1b; Fig. S2), consistent with the notion that proximal neural elements are more similar to one another [47, 60, 67, 120, 137]. However, there is variability in how feature similarity decreases with distance. For instance, dynamic modes demonstrate stronger exponential relationships whereas molecular modes demonstrate either weak exponential or linear (in the case of laminar similarity) fits.

We next sought to relate each connectivity mode to the brain's underlying structural architecture. We constructed a weighted structural connectome using diffusion-weighted MRI data from the Human Connectome Project; this network represents whether, and how much, two brain regions are connected by white mat-
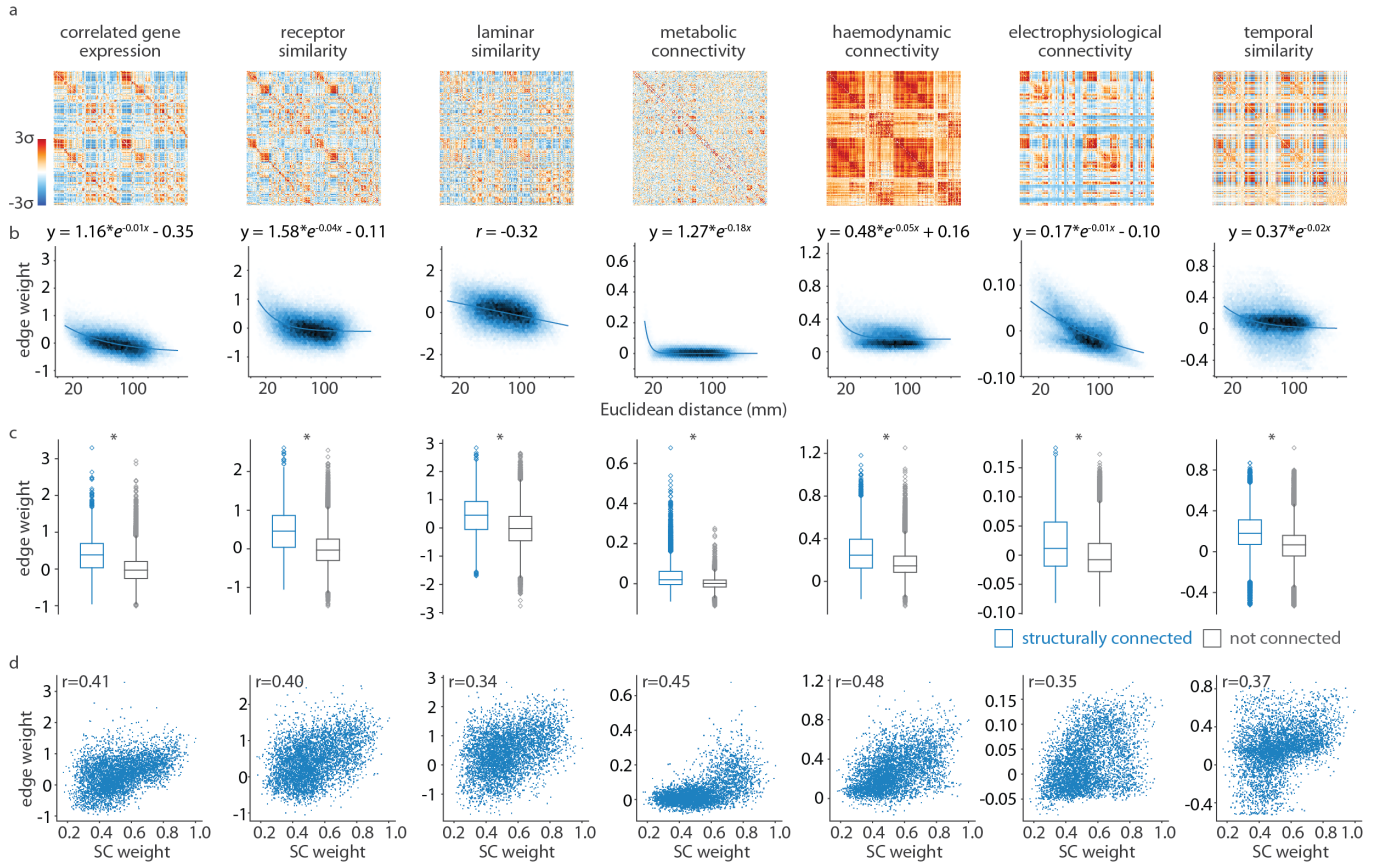
Figure 1. Common organizational principles of connectivity modes | Each connectivity mode is represented as a normalized similarity matrix, where elements of the matrix index how similarly two brain regions present a specific feature. (a) Connectivity modes are shown as heatmaps, ordered according to the 400-region Schaefer parcellation [129]. The colourbar limits are −3 to 3 standard deviations of the edge weight distribution. (b) Edge weights between every pair of brain regions (i.e. upper triangular elements) decrease with Euclidean distance across all seven connectivity modes. Darker colour represents greater density of points. Exponential equations or Spearman correlation coefficients are shown depending on whether the relationship is better fit by an exponential or linear function. Similar relationships with geodesic distance are shown in Fig. S2. (c) Edge weight distributions are visualized separately for edges that also exist in the structural connectome (blue) and those that do not (grey), according to a group-consensus structural connectome from the HCP [160]. Structurally connected brain regions show greater similarity than regions that are not structurally connected. Boxplots represent the 1st, 2nd (median) and 3rd quartiles, whiskers represent the non-outlier end-points of the distribution, and diamonds represent outliers (> 1.5 inter-quartile range). (d) For edges that also exist in the structural connectome, connectivity mode edge weight increases with the strength of the structural connection.

ter streamlines. We find that, across all seven connectivity modes, brain regions that are physically connected by white matter show greater feature similarity than those that are not connected, suggesting that biologically similar neuronal populations are in direct communication (Fig. 1c). These differences are greater than in a population of degree- and edge length-preserving surrogate structural connectomes, indicating that the effect is specifically due to wiring rather than spatial proximity [21]. Finally, for the subset of edges with a structural connection, we find a correlation between the strength of the structural connection and each connectivity mode's edge weight (Fig. 1d) [70]. Altogether, we find that connectivity modes demonstrate common organizational principles that respect geometry, neuroanatomy, and anatomical connectivity, regardless of imaging modality or biological mechanism.

Structural and geometric features of connectivity modes

Although connectivity modes share organizational properties, the median correlation between them is $r = 0.25$ (range: $r = 0.10$–0.53; Fig. S3). In other words, connectivity modes are not redundant. To directly compare edge weights across connectivity modes, we converted edge weights to ranks, such that the smallest (i.e. most negative) edge is ranked 1 and the strongest (i.e. most positive) edge is ranked 79 800 (equal to the number of edges in each network). We focus on two metrics to clas-
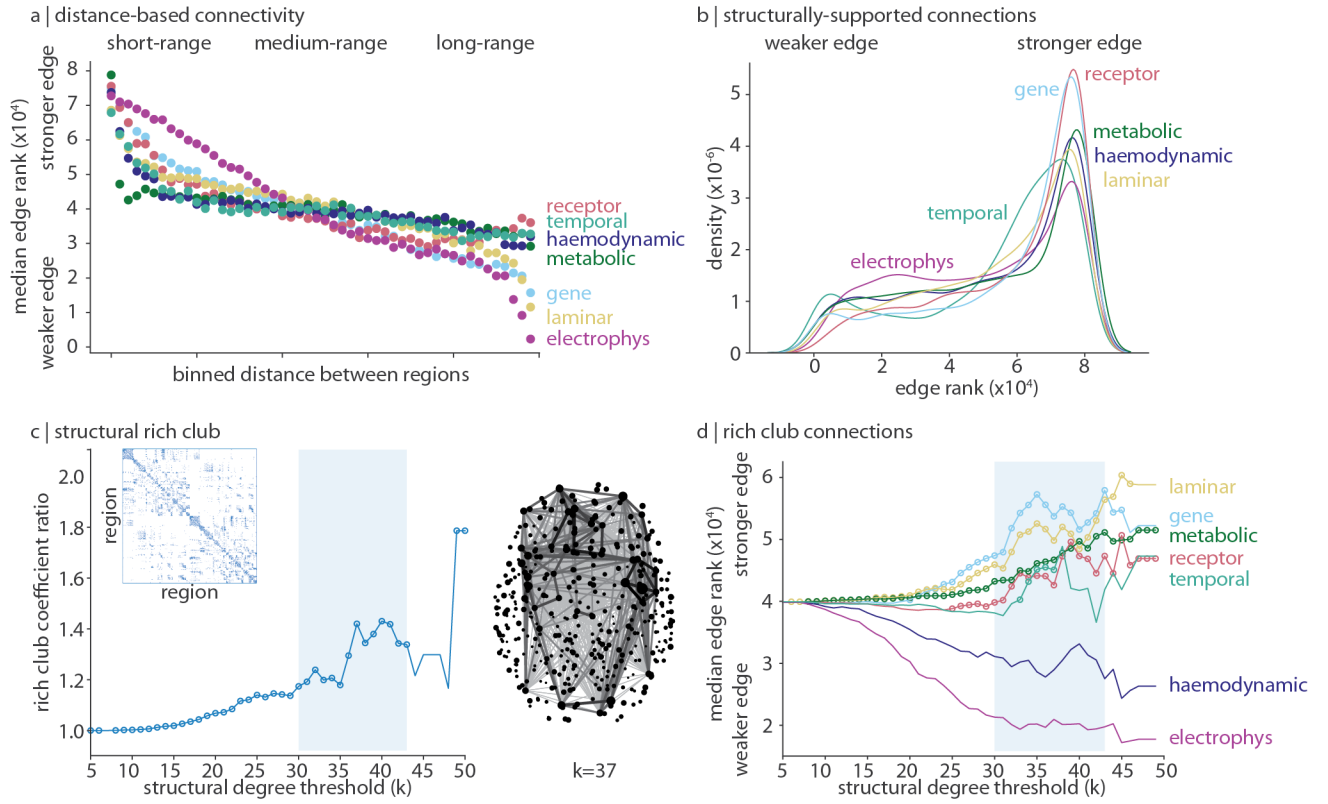
a | distance-based connectivity

short-range   medium-range   long-range

median edge rank (x10⁴) — stronger edge / weaker edge

binned distance between regions

receptor
temporal
haemodynamic
metabolic
gene
laminar
electrophys

b | structurally-supported connections

weaker edge   stronger edge

density (x10⁻⁶)

edge rank (x10⁴)

receptor
gene
metabolic
haemodynamic
laminar
temporal
electrophys

c | structural rich club

rich club coefficient ratio

region / region

structural degree threshold (k)

k=37

d | rich club connections

median edge rank (x10⁴) — stronger edge / weaker edge

structural degree threshold (k)

laminar
gene
metabolic
receptor
temporal
haemodynamic
electrophys

Figure 2. **Structural and geometric features of connectivity modes |** To compare edge weights across networks, edges are rank-transformed. (a) Edges are binned into 50 equally-sized bins of increasing Euclidean distance (1 596 edges per bin). For each connectivity mode, the median edge rank is plotted within each bin. (b) A kernel density estimation is applied on the rank-transformed feature similarity (edge rank) distribution of edges that also have a structural connection, for each connectivity mode. (c) For a structural degree threshold $k \in [5, 50]$, we calculate the rich club coefficient ratio and show a characteristic increase in rich club coefficient ratio when $30 \leq k \leq 43$. Circles indicate structural degree thresholds where the rich club coefficient ratio is significantly greater than a null distribution of ratios calculated using a degree-preserving rewired network (1 000 repetitions). On the right we show the set of structural edges connecting regions with structural degree ≥ 37. Edge shade and thickness are proportional to edge weight, and point size is proportional to structural degree. The binary structural connectome is shown in the inset. (d) For each $k \in [5, 50]$ and for each connectivity mode, we calculate the median edge rank of structurally-supported edges that connected regions with structural degree $\geq k$. Circles indicate structural degree thresholds where the median rich-link edge rank of a connectivity mode is significantly greater than the edge rank of all other structurally-supported edges (Welch's t-test, one-sided).

sify edges between brain regions: distance and structural connectivity.

Spatial proximity influences inter-regional similarity, such that proximal regions tend to share similar biological and physiological features (Fig. 1b, [21, 146]. We therefore sought to investigate how distance shapes inter-regional feature similarity in greater detail and in a comparative manner. We first bin all 79 800 edges into fifty equally-sized bins (1 596 edges per bin). For each connectivity mode separately, we calculate the median edge rank within each bin (Fig. 2a). Median edge rank decreases as the distance between brain regions in each bin increases, consistent with our finding in Fig. 1b. We find two broad patterns: receptor similarity, temporal similarity, haemodynamic connectivity, and metabolic connectivity show moderate decrease of

edge strength with distance, whereas correlated gene expression, laminar similarity, and especially electrophysiological connectivity demonstrate a sharper decrease of edge strength with distance. In other words, distance plays a unique role in shaping each individual connectivity mode, with electrophysiological connectivity, laminar similarity, and correlated gene expression being most influenced by distance. That receptor similarity is grouped with predominantly dynamic modes (haemodynamic, metabolic, and temporal similarity) may reflect the influence that receptor density has on brain dynamics.

We next shift our focus to the subset of edges with an anatomical connection, according to the structural connectome ($N = 4\,954$ out of 79 800 edges). For each connectivity mode, we plot the distribution of rank-transformed feature similarity (edge rank) for
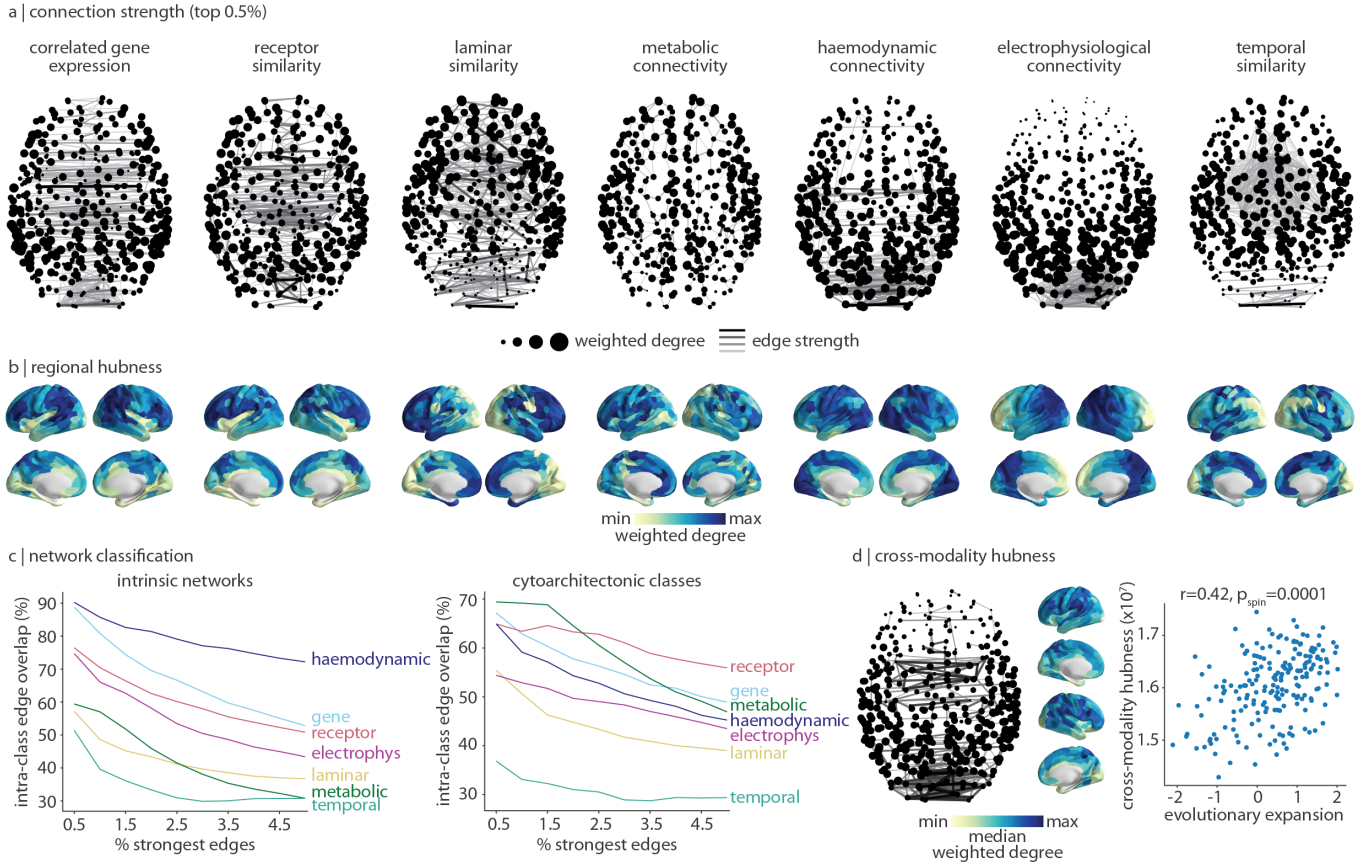
a | connection strength (top 0.5%)

correlated gene expression · receptor similarity · laminar similarity · metabolic connectivity · haemodynamic connectivity · electrophysiological connectivity · temporal similarity

● ● ● weighted degree ≡ edge strength

b | regional hubness

min ▬ max
weighted degree

c | network classification

intrinsic networks

cytoarchitectonic classes

d | cross-modality hubness

min ▬ max
median weighted degree

$r=0.42$, $p_{spin}=0.0001$

Figure 3. **Cross-modal hubs** | (a) For each connectivity mode, we plot the 0.5% strongest edges. Darker and thicker edges indicate stronger edges. Points represent brain regions and are sized according to the sum of edge weights (weighted degree). Brain views are axial, with anterior regions at the top of the page (for coronal and sagittal views, see Fig. S4). (b) For each connectivity mode, regional hubness is defined as the sum of rank-transformed edge weights across regions. (c) For a varying threshold of strongest edges (0.5%–5% in 0.5% intervals), we calculate the proportion of edges that connect two regions within the same intrinsic network (left [172]) and cytoarchitectonic class (right [166]). (d) Across all seven connectivity modes, we calculate the median edge rank of each edge and plot the 0.5% strongest edges (left). Likewise, we calculate the median hubness (shown in panel b), which we find is significantly correlated with evolutionary cortical expansion ($r = 0.42$, $p_{spin} = 0.0001$) [68].

these edges that also exist in the structural connectome (Fig. 2b). This lets us determine which connectivity modes demonstrate the greatest coupling between high inter-regional feature similarity and structural connectivity: namely, receptor similarity and correlated gene expression. This serves as the first indication that molecular connectivity modes tend to conform most to structural connections. The primacy of molecular connectivity modes is a finding that returns in the next analysis and when we compare connectivity modes to disease pathology (*Connectivity modes shape disease vulnerability*).

We next track how edge strength changes depending on the structural embedding of each brain region. We focus on the brain's rich club: a set of disproportionately interconnected high-degree brain regions that is thought to mediate long-range information propagation and integration [50, 157]. Is this rich club architecture supported by specific biological and physiological features? To address this question, for each struc-

tural degree threshold $k \in [5, 50]$ (where structural degree is defined as the number of structural connections made by a brain region), we calculate the rich club coefficient ratio on the binary structural connectome: the tendency for brain regions of degree $\geq k$ to be preferentially connected to one another, with respect to a population of degree-preserving surrogate networks. We find that the rich club coefficient ratio is inflated at approximately $30 \leq k \leq 43$, suggesting the existence of rich club organization (Fig. 2c). This topological rich club regime denotes a degree range where brain regions are unexpectedly densely interconnected [35]. Next, for each connectivity mode at each k, we calculate the median edge rank of all structurally-supported edges that link two brain regions with degree $\geq k$ (Fig. 2d). Moreover, we ask whether within-set edge ranks (i.e. edges connecting regions with degree $\geq k$) are statistically greater than all other edges (Welch's one-sampled t-test).

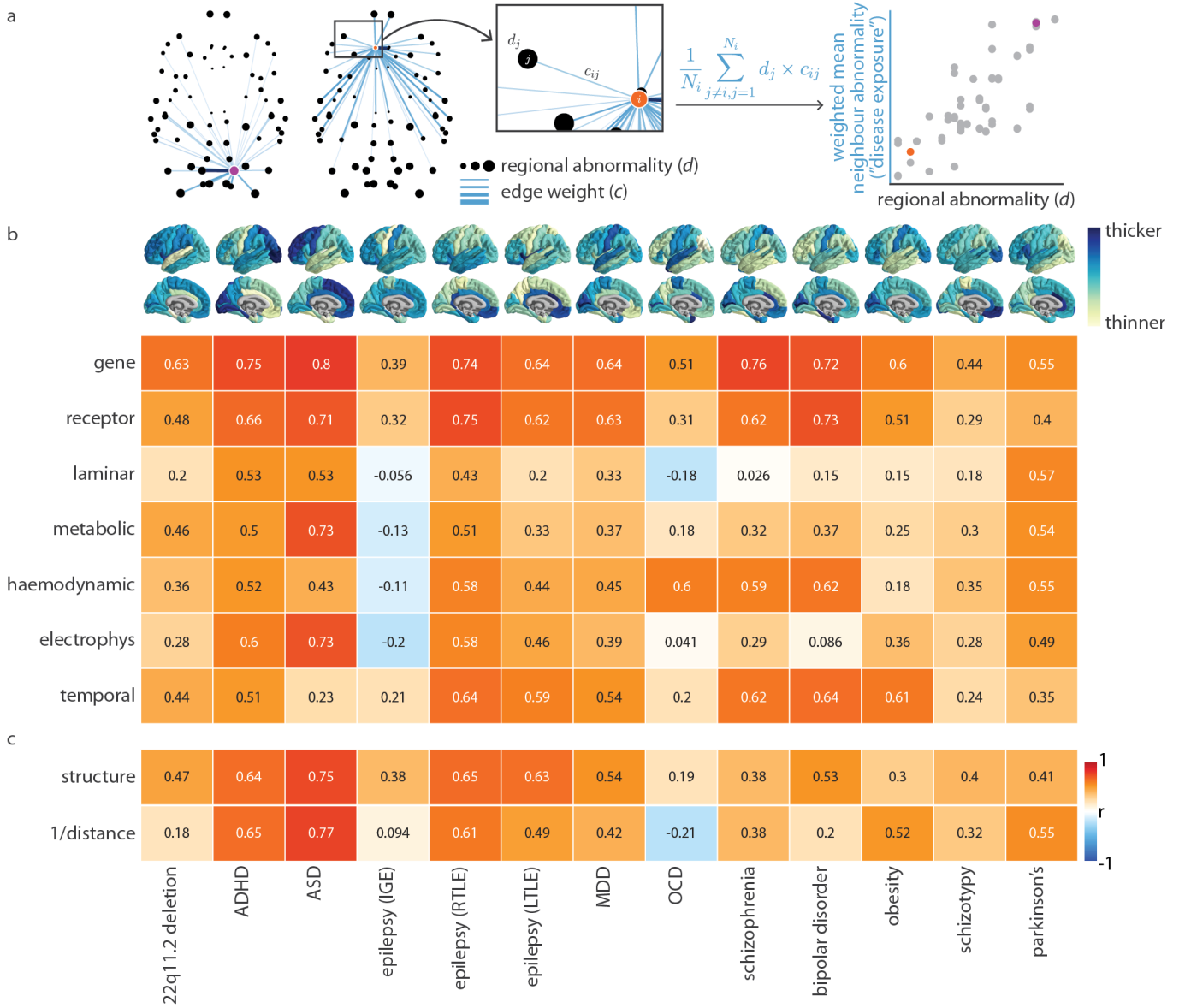We find that edges in the brain's topological rich club

Figure 4. **Contributions of connectivity modes to disease vulnerability |** Cortical abnormality profiles for thirteen neurological, psychiatric, and neurodevelopmental disorders were collected from the ENIGMA consortium (brain plots shown in panel b; $N = 21\,000$ patients, $N = 26\,000$ controls [85, 151]). (a) Given a specific disorder and connectivity mode, d_j represents the cortical abnormality of region j, and c_{ij} represents the edge weight (similarity) between regions i and j. For every region i, we calculate the average cortical abnormality of all other regions $j \neq i$ in the network, weighted by the edge strength ("disease exposure"); note that we omit negative connections, such that N_i represents the number of positive connections made by region i). Next, we correlate disease exposure and regional abnormality across brain regions (scatter plot; points represent brain regions). We show the connectivity profiles of two example regions (highlighted in purple in the left brain network and orange in the right brain network). (b) The analytic workflow presented in panel a is repeated for each disorder and connectivity mode, and we visualize Spearman correlations in a heatmap. (c) This analysis is repeated for weighted structural connectivity (where we only consider structurally-connected regions), and Euclidean distance (where we always consider all regions in the network).

regime are particularly dominated by molecular features (e.g. laminar similarity, correlated gene expression, and receptor similarity). Haemodynamic and electrophysiological connectivity are especially weak for links between high-degree regions, and temporal similarity is unstable. Metabolic connectivity is an additional connectiv-ity mode that demonstrates significantly increased edge strength for links between high-degree regions, suggesting that energy consumption is synchronized between structural hubs [5, 50, 87, 155]. Collectively, these results point to the possible biological origins of the rich club. Namely, the rich club may reflect coordinated pat-
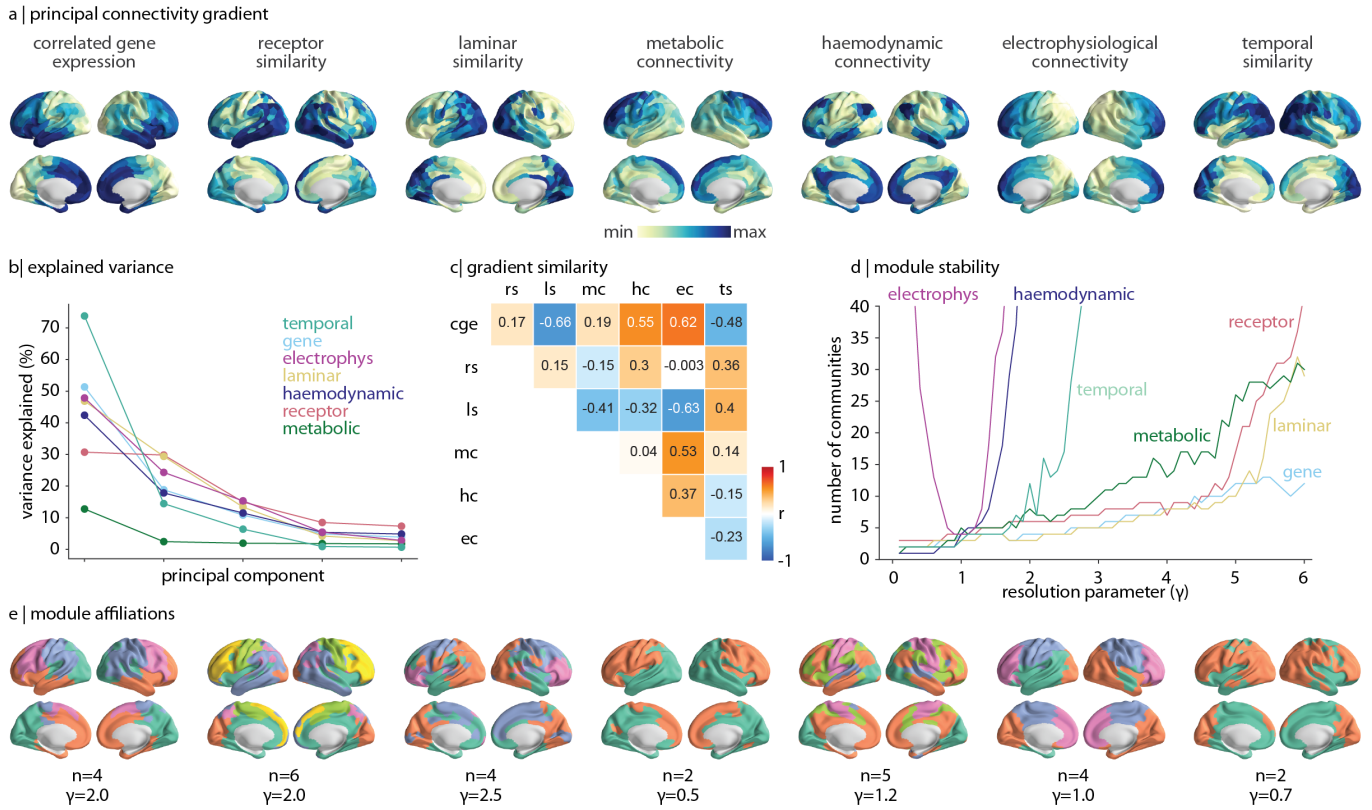
a | principal connectivity gradient

correlated gene expression | receptor similarity | laminar similarity | metabolic connectivity | haemodynamic connectivity | electrophysiological connectivity | temporal similarity

min ▭ max

b| explained variance

c| gradient similarity

d | module stability

e | module affiliations

n=4 γ=2.0 | n=6 γ=2.0 | n=4 γ=2.5 | n=2 γ=0.5 | n=5 γ=1.2 | n=4 γ=1.0 | n=2 γ=0.7

Figure 5. **Gradients and modules of connectivity modes |** (a) The first principal component ("gradient") of each connectivity mode is shown on the cortex. (b) The percent variance explained for the first five principal components of each connectivity mode. (c) The Pearson's correlation between every pair of network gradients, visualized as a heatmap. CGE=correlated gene expression, RS=receptor similarity, LS=laminar similarity, MC=metabolic connectivity, HC=haemodynamic connectivity, EC=electrophysiological connectivity, TS=temporal similarity. (d) The Louvain community detection algorithm is applied to each connectivity mode across different resolution parameters ($0.1 \leq \gamma \leq 6.0$, in intervals of 0.1) and the number of ensuing communities is plotted as a function of γ. (e) For each connectivity mode we show a single community detection solution for a specified γ, and we indicate the number of communities (n).

terns of inter-regional microscale similarity. On the other hand, the rich club is not characterised by similar neural dynamics, possibly related to the functional flexibility of these regions [57].

Cross-modal hubs

Mapping hubs in the human brain has been a topic of great interest in the last 15 years, but the majority of our knowledge comes from anatomical and haemodynamic connectivity [144, 158]. For a more comprehensive understanding of brain regions that make many strong connections, it would be important to map their connectivity profiles at different levels of organization. We therefore ask whether there exist edges that are consistently high-strength, and if so, which brain regions, which we call cross-modal hubs, make these connections. For every connectivity mode, we show an axial view of the 0.5% strongest edges (Fig. 3a, see Fig. S4 for coronal and sagittal views). Interestingly, high-strength edges vary

across connectivity modes: some networks form densely interconnected cores (i.e. electrophysiological connectivity and temporal similarity), some emphasize long-range (i.e. haemodynamic connectivity) or short-range (i.e. metabolic connectivity) connections, and others appear more non-specific (i.e. correlated gene expression, receptor similarity, and laminar similarity; Fig. 3a). This variability is also reflected in the hubness profiles of each connectivity modality, where a brain region's hubness is defined as the sum of the rank-transformed edge weights between it and all other regions (Fig. 3b). The variability of hubness points to the importance of characterizing network architecture from multiple complementary perspectives.

Are there consistencies in high-strength edges and regions? Previous work has shown that the brain can be organized into modules of regions that are either functionally similar ("intrinsic networks" [172]) or cellularly similar ("cytoarchitectonic classes" [164, 166]). We wanted to know whether connectivity modes across multiple scales emphasize edges that link brain regions within

these functional and cytoarchitectonic networks, regardless of whether the connectivity mode represents brain function or cellular composition. For a given network classification (e.g. intrinsic networks), we call edges that join two brain regions in the same network (e.g. the visual network) intra-class edges [134]. We then calculate how many of the x strongest edges in a given connectivity mode overlap with intra-class edges. We let x vary in increments of 0.5% from 0.5% to 5% of the strongest edges in a connectivity mode.

For intrinsic networks (Fig. 3c, left), the strongest edges in the haemodynamic network are almost entirely intra-class edges (90.2% for the top 0.5% strongest edges, and 72.2% for the top 5% edges). The strongest edges in correlated gene expression are also primarily intra-class edges (88.7% for the top 0.5% strongest edges) but this ratio decreases to 52.8% at 5% of the strongest edges. Meanwhile, for cytoarchitectonic classes (Fig. 3c, right), receptor similarity, correlated gene expression, and metabolic connectivity most maximize intra-class edges. Across both intrinsic and cytoarchitectonic networks, temporal similarity retains the fewest intra-class edges. Nonetheless, the negative slopes in Fig. 3c indicates that, for every connectivity mode, strongest edges are preferentially edges that connect brain regions within the same functional and cytoarchitectonic network (Fig. 3c). More generally, when we consider the median edge rank across all connectivity modes, we find that consistently high-strength edges primarily connect visual, posterior parietal, and anterior temporal regions (Fig. 3d, left).

Finally, we focus on the brain regions: are there regions that are similar to many other regions with respect to multiple different microscale properties? We quantify cross-modal hubness as the median hubness across connectivity modes (i.e. the median across brain plots shown in Fig. 3b). We find that transmodal regions such as the supramarginal gyrus, superior parietal cortex, precuneus, and dorsolateral prefrontal cortex are most consistently similar to other brain regions across all connectivity modes (Fig. 3d, right). Interestingly, these transmodal regions are commonly thought of as structural hubs but here we show that they are central at multiple levels of organization.

Why are some brain regions highly similar to many other regions across multiple spatial scales and biological mechanisms? We hypothesized that cross-modal hubs are more cognitively flexible and able to support higher-order, evolutionarily-advanced cognitive processes. We therefore correlated cross-modal hubness with a map of evolutionary cortical expansion [68]. Indeed, the identified cross-modal core coincides with brain regions that are more expanded across phylogeny ($r = 0.43$, $p_{\text{spin}} = 0.0001$). In other words, brain regions that are expanded in humans and therefore likely involved in higher-order cognition share many features across multiple scales, suggesting they can integrate signals from a more diverse set of neural circuits. Ultimately, hubs that

are defined using connectivity modes other than the classical structural connectome provide novel perspectives on how regions participate in neural circuits.

Connectivity modes shape disease vulnerability

We next ask how connectivity modes shape the spatial patterning of brain diseases. Emerging theories emphasize that the course and expression of multiple brain diseases is mediated by shared molecular vulnerability [61, 169]. To address this hypothesis, we compared connectivity modes with patterns of cortical abnormalities across thirteen different neurological, psychiatric, and neurodevelopmental diseases and disorders from the ENIGMA consortium ($N = 21\,000$ patients, $N = 26\,000$ controls) [61, 85, 151].

We define the "exposure" that region i has to region j's pathology as the product between the (i, j)-edge strength (c_{ij}) and region j's abnormality (d_j) (Fig. 4a) [32, 61, 136, 138]. Then the global disease exposure to region i is the mean exposure between region i and all other regions in the network with positive edge strength. Finally, we correlate cortical abnormality with disease exposure to determine whether the spatial patterning of the disease is informed by a connectivity mode (Fig. 4a, right). This analysis is repeated for each connectivity mode and each disorder, and correlation coefficients are visualized in Fig. 4b.

We find that correlated gene expression and receptor similarity most consistently amplify the exposure of pathology in a manner that closely resembles the cortical profile of the disease. This suggests that brain regions with similar molecular makeup may undergo similar structural changes in disease [132]. By repeating the analysis using weighted structural connectivity (in which case we only consider structurally-connected regions) and Euclidean distance between brain regions (in which case we always consider the full network), we are able to uncover cases where feature similarity amplifies disease exposure more than structure or distance alone (Fig. 4c). Cortical abnormality patterns of psychiatric disorders in particular (e.g. MDD, schizophrenia, bipolar disorder, OCD) are better explained by correlated gene expression and receptor similarity than structure or distance. This integrative analysis makes it possible to hone in on the imaging modalities and biological mechanisms that might most reflect cortical pathology; in this case, bringing to light the relevance of molecular rather than dynamic modes in psychiatric disorders.

Gradients and modules of connectivity modes

We next consider how each connectivity mode is intrinsically organized, both in terms of axes of variation (i.e. spatial gradients) and network modules [38, 59, 94, 112]. Principal gradients have been extensively studied
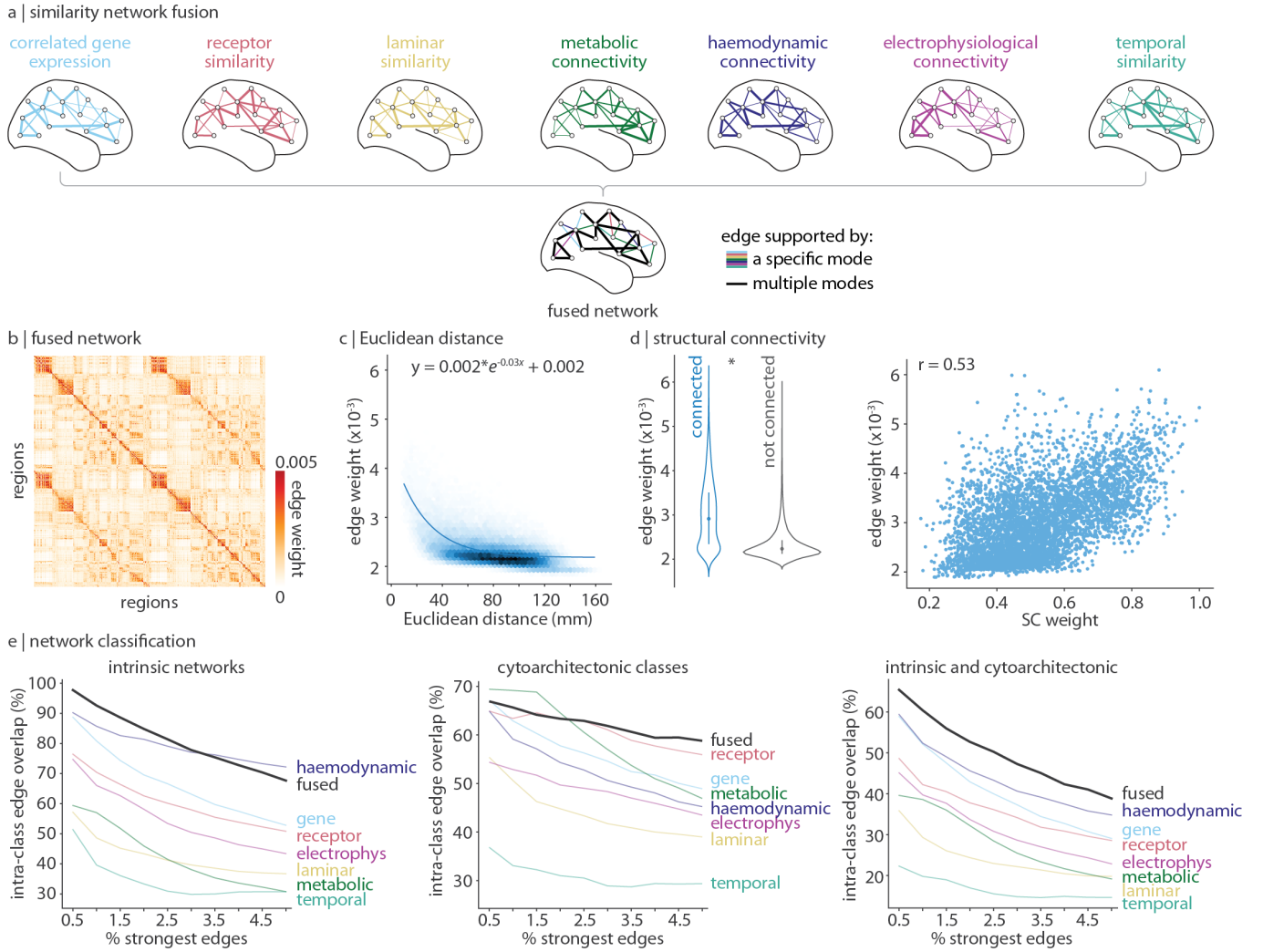
Figure 6. **Network fusion |** Similarity network fusion was applied to all seven connectivity modes to construct a single integrated network [98, 168]. (a) Toy example of similarity network fusion (SNF). SNF iteratively combines the seven connectivity modes in a manner that gives more weight to edges between observations that are consistently high-strength across data types (black edges). (b) The fused network. (c) Edge weight decreases exponentially with Euclidean distance. (d) Structurally connected edges have greater edge weight than edges without an underlying structural connection, against a degree and edge-length preserving null model (left [21]), and is correlated with structural connectivity (right). (e) For a varying threshold of strongest edges (0.5%–5% in 0.5% intervals), we calculate the proportion of edges that connect two regions within the same intrinsic network (left), cytoarchitectonic class (middle), and the union of intrinsic networks and cytoarchitectonic classes (right).

in the literature [20], although the amount of variance explained by the gradient is under-appreciated compared to its spatial patterning. Here we show that the prominence of the first gradient can vary substantially across connectivity modes (Fig. 5a). For example, the temporal similarity gradient is especially dominant (accounting for 73.8% of variance) while the metabolic connectivity gradient is especially non-dominant (accounting for 12.7% of variance; Fig. 5b). Furthermore, we find that brain gradients do not all follow a uniform sensory-association axis [73, 96, 149], rather, the first principal component of each connectivity mode varies considerably (median absolute correlation between gradients

$r = 0.36$; Fig. 5c).

An alternative perspective of intrinsic network organization comes from considering whether and how the network clusters into segregated modules. We apply the Louvain community detection algorithm to each connectivity mode and, across a range of resolution parameter values (γ), extract community assignments for each brain region [12, 23]. To get a sense of the resolution of each network (i.e. the number of communities the network might naturally exhibit, if at all), we track the number of communities identified by the Louvain community detection algorithm across different values of γ (Fig. 5d). We find that the community detection solution

for electrophysiology is highly unstable, with the number of identified communities changing rapidly with small changes in γ. The most stable solution at $\gamma = 1$ simply delineates the main cortical lobes. Haemodynamic connectivity and temporal similarity show a similar trend, where partitions of greater than approximately 5 networks become increasingly unstable. Meanwhile, correlated gene expression, laminar similarity, and receptor similarity show more stable community solutions, where larger changes in γ are required for the network to split itself into more communities. We show one possible consensus community detection solution for each network in Fig. 5e, which demonstrates that the modular organization and gradient decomposition of networks tend to be closely aligned. Collectively, this shows that each connectivity mode has a unique gradient decomposition and community structure.

Fusing connectivity modes

Each connectivity mode that we have studied so far represents a single scale of organization describing distinct but related inter-regional relationships. Given that the brain is integrated, how do these connectivity modes layer onto one another to support brain structure and function? To address this questions, we apply an unsupervised learning technique, similarity network fusion (SNF), to merge all seven connectivity modes into a single multimodal network (Fig. 6a) [168]. SNF iteratively fuses each connectivity mode in a manner that strengthens edges that are consistently strong and weakens inconsistent (or consistently weak) edges, while giving each connectivity modality equal influence on the fusion processes. Altogether, the fused network represents a data-driven integration of each level of brain connectivity.

The fused network exhibits non-random network organization including strong homotopic connectivity and a negative exponential relationships with distance (Fig. 6b, c). In addition, structurally connected edges have significantly stronger edge weight than non-connected edges, against a degree- and edge-length preserving structural null (Fig. 6d). Finally, the fused network demonstrates a greater correlation between edge weight and weighted structural connectivity than any of the individual connectivity modes ($r = 0.53$). This shows how combining inter-regional similarity across multiple scales can be used to better explain anatomical connectivity [147].

We next asked whether the strongest edges in the fused network exist between functionally and cytoarchitectonically similar brain regions (Fig. 6e). We find that nearly all (97.7%) of the top 0.5% strongest edges in the fused network are between regions within the same functional network. In fact, the fused network outperforms haemodynamic connectivity—the connectivity mode for which these intrinsic functional networks are designed and optimized. Likewise, for cytoarchi-

tectonic classes, we find that the fused network retains more intra-class edges than any other network when the number of strongest edges considered is $\geq 2.5\%$. Since the fused network represents an integrated connectivity mode, we asked whether the strongest edges of the fused network might simultaneously maximize intrinsic and cytoarchitectonic intra-class edges. Indeed, when considering the top 0.5% to 5.0% strongest edges, the number of edges that exist between regions in the same intrinsic and cytoarchitectonic classes is consistently greatest for the fused network. Altogether, the fused network maps onto intrinsic networks and cytoarchitectonic classes better than any individual network. This demonstrates how large scale phenomena emerge from a confluence of multiple microscopic determinants.

Sensitivity and replication analysis

Finally, to ensure results are not dependent on the parcellation, we repeated all analyses (except Fig. 4 which depends on the 68-region Desikan-Killiany parcellation) using the 100-region Schaefer parcellation and the 68-region Desikan-Killiany parcellation [30, 39, 129]. We find similar results under these alternative parcellations (Fig. S5). These coarser resolutions reveal dense frontal inter-connectivity in the metabolic network, which was not visible at the 400-node parcellation likely due to smoothing effects in dynamic PET data. Furthermore, we share all seven connectivity modes at these three parcellations (Schaefer-400, Schaefer-100, Desikan-Killany-68) in hopes of facilitating integrative connectome analyses in the future (https://github.com/netneurolab/hansen_many_networks).

DISCUSSION

This work integrates multiple representations of brain connectivity to establish how diverse connectivity modes contribute to brain structure and function. We systematically document the common organizational principles of connectivity modes, as well as their unique contributions to brain structure and geometry. We find that molecular connectivity modes amplify disease exposure resulting in spatial patterns of cortical abnormality. We show that connectivity modes demonstrate diverse dominant gradients and modular structure. Finally, we derive a multimodal, multiscale network by parsimoniously integrating multiple connectivity modes.

Connectomics—the study of relationships between neural elements across multiple scales—is increasingly becoming the dominant paradigm in neuroscience [13, 88, 145]. Numerous technological and analytic methods have been developed to reconstruct inter-regional relationships, some focused on physical wiring, others on molecular similarity, and others still on coherence between regional neural activity. Despite being rooted in

common questions, these connectivity modes are often studied in separate literatures. What network features are unique or common to each connectivity mode remains unknown and the practice of studying connectivity modes separately has precluded a truly integrated understanding of inter-regional relationships.

Detailed comprehensive datasets alongside better data sharing practices have made multi-modal, integrative approaches to studying human brain connectivity more feasible [42, 86, 96, 167]. Examples include comparisons of dynamic FDG-PET and BOLD connectivity [75, 165], BOLD connectivity and electrophysiology [25, 26, 64, 135], structural and BOLD connectivity [70, 156], and correlated gene expression and structural connectivity [122]. Combining connectivity modes has also been used to better resolve clusters of functional activation in BOLD data [93], and inform the application of deep brain stimulation to psychiatric and neurological diseases [11, 72]. Encouragingly, previous work has found that incorporating multiple perspectives of brain connectivity can result in novel discoveries, including improved generative models of brain connectivity [110], structure-function coupling [60, 114], epicentres of transdiagnostic alterations [61, 65], and the characterization of homophilic wiring principles [16].

Although these integrative approaches open exciting new questions about brain organization, an important challenge remains: how do we ensure that conclusions are rooted in the underlying biology rather than assumptions and idiosyncrasies of individual data modalities? We attempted to mitigate this challenge by repeating analyses using other analytic choices, applying conservative null models, normalizing each connectivity mode prior to analysis (Fisher's r-to-z transformation), and rank-transforming edges to facilitate comparison of edge strengths across data types. This provides a level of confidence but is by no means an exhaustive verification that data types do not influence results. Indeed, each dataset is accompanied by its own set of limitations including instances of false positives and negatives in diffusion tractography [78, 91, 174], non-specific binding for some PET tracers [46], and heterogeneous patterns of signal to noise ratios across all imaging types. As open datasets are created and shared, it will become more feasible to determine how results are influenced by processing choices and imaging modalities.

The study of connectomics has been dominated by a focus on structural and haemodynamic connectivity. This has resulted in the assumption that homologous [121], spatially proximal [47], and structurally connected [67] brain regions tend to be more similar. By systematically integrating seven multi-scale perspectives of brain connectivity, we show that these properties are indeed fundamental to brain organization but that there is considerable variation across connectivity modes. For example, the negative exponential relationship with distance is almost linear for molecular connectivity modes, especially when we consider geodesic instead of Euclidean distance

(Fig. S2). A second assumption, this stemming primarily from fMRI studies, is that the brain ubiquitously follows a unimodal-transmodal hierarchical gradient, and can be organized in terms of intrinsic resting-state networks. However, we find diverse gradient decompositions and community structures across spatial scales and biological mechanisms. Furthermore, we find that microscale connectivity modes (e.g. correlated gene expression, receptor similarity) are well delineated by a partition based on cytoarchitectonic classes whereas dynamic connectivity modes (e.g. haemodynamic connectivity, electrophysiological connectivity) fit better into intrinsic cognitive systems. Indeed, connectivity modes are poorly correlated with one another, suggesting that each connectivity mode provides a fundamentally different but important view of how brain regions participate in neural circuits at different spatial and temporal scales [15].

In an effort to understand which brain regions are consistently central across many levels of description, we identify a set of cross-modal hubs. Brain hubs are conventionally defined as regions with a relatively large number of structural connections, but this definition ignores the multiscale character of brain networks. Indeed, we find that hub profiles are not redundant across biological mechanisms. Instead, we identify a subset of brain regions that are uniquely central across multiple levels of description. These cross-modal hubs exist in the precuneus, supramarginal gyrus, and dorsolateral prefrontal cortex: association regions that most expand during evolution and are involved in high-level cognition including language, planning, and complex executive functions [68, 171]. This may indicate that these functions are supported by integration across multiple biological scales. Altogether, cross-modal hubs open a new perspective on hub function: instead of being rooted only in high structural connectivity, hubs can be classified according to their participation in different biological systems [5].

Integrative connectomics opens the possibility of benchmarking and comparing biological mechanisms to one another. For example, we consistently identify a dichotomy between molecular (e.g. correlated gene expression, receptor similarity, laminar similarity) and dynamic (e.g. haemodynamic and electrophysiological connectivity) modes. First, molecular feature similarity is significantly increased for links between regions of the brain's rich club: high-degree regions that show dense inter-connectivity which is thought to improve global communication efficiency and integration [157]. A transcriptional signature of rich club connectivity was previously shown to be driven by genes involved in metabolism, supporting the theory that the brain's rich club is energetically expensive [28, 36, 50]. Interestingly, we find that metabolic connectivity is increased in rich links, suggesting that the rich club is also synchronized in its energy consumption [87, 155].

Second, molecular feature similarity—particularly correlated gene expression and receptor similarity—best explains the spatial patterning of multiple cortical dis-

ease abnormalities. Recent work has explored the idea that multiple pathologies spread trans-synaptically, including misfolded proteins, aberrant neurodevelopmental signals, and excitotoxic electrical discharge, resulting in patterns of pathology that reflect the underlying structural architecture of the brain [138, 175]. Here we consider the possibility that shared vulnerability to disease arises not just from structural connectivity but also from multiscale biological attributes [61]. We use changes in cortical thickness as the marker of potential pathology and find that when disease exposure is informed by transcriptional and receptor similarity, we can reproduce the cortical profile of multiple diseases ($r > 0.5$ for most). The consistent primacy of molecular connectivity modes demonstrates that mapping brain connectivity from the perspective of the underlying biology—gene transcription, receptor density, cellular composition—is just as, if not more, informative than oft-studied dynamical modes such as haemodynamic connectivity.

The present work should be considered alongside some methodological considerations. First, the results are only representative of the seven included connectivity modes; future work should extend this work into additional forms of connectivity. One exciting avenue would be to annotate structural connectomes with measures of myelin or axon caliber derived from quantitative MRI such as magnetization transfer (MT), T1 relaxation rate (R1), or axon diameter [7, 90, 106]. Second, each connectivity matrix is dependent on the quality of the imaging modality, and each imaging method operates at a unique spatial and temporal resolution. Results may therefore be influenced by differences in how the data are acquired. We tried to mitigate this by running extensive sensitivity analyses. Third, in an effort to make correlated gene expression comparable to the other modes, data interpolation and mirroring was conducted, potentially biasing this network towards homotopic connections. Fourth, connectivity modes are compiled across different individuals of varying ages and sex ratios. Results are therefore limited to group-averages, and motivate future deep phenotyping studies of the brain across multiple scales and modalities.

Altogether, this work combines seven perspectives of brain connectivity from diverse spatial scales and imaging modalities including gene expression, receptor density, cellular composition, metabolic consumption, haemodynamic activity, electrophysiology, and time-series features. We demonstrate both the similar and complementary ways in which connectivity modes reflect brain geometry, structure, and disease. This serves as a step towards the next-generation integrative, multimodal study of brain connectivity.

METHODS

Connectivity modes

We construct cortical connectivity modes for seven different brain features: gene expression, receptor density, lamination, glucose uptake, haemodynamic activity, electrophysiological activity, and temporal profiles. Each connectivity mode is defined across 400 cortical brain regions, ordered according to 7 intrinsic networks (visual, somatomotor, dorsal attention, ventral attention, limbic, frontoparietal, default mode), separated by hemispheres (left, right) [129]. Replication analyses were conducted using the 100-region Schaefer and 68-region Desikan-Killiany parcellations (all available at https://github.com/netneurolab/hansen_many_networks). To facilitate comparison between connectivity modes, each connectivity mode is normalized using Fisher's r-to-z transform ($z = \operatorname{arctanh}(r)$). We describe the construction of each connectivity mode in detail below.

Correlated gene expression

Correlated gene expression represents the transcriptional similarity between pairs of brain regions. Regional microarry expression data were obtained from 6 post-mortem brains (1 female, ages 24.0–57.0, 42.50 ± 13.38) provided by the Allen Human Brain Atlas (AHBA, https://human.brain-map.org [63]). Data were processed with the abagen toolbox (version 0.1.1; https://github.com/rmarkello/abagen [95]) using a 400-region volumetric atlas in MNI space.

First, microarray probes were reannotated using data provided by Arnatkevičiūtė et al. [6]; probes not matched to a valid Entrez ID were discarded. Next, probes were filtered based on their expression intensity relative to background noise [116], such that probes with intensity less than the background in $\geq 50\%$ of samples across donors were discarded , yielding $31\,569$ probes. When multiple probes indexed the expression of the same gene, we selected and used the probe with the most consistent pattern of regional variation across donors (i.e., differential stability [62]), calculated with:

$$\Delta_S(p) = \frac{1}{\binom{N}{2}} \sum_{i=1}^{N-1} \sum_{j=i+1}^{N} r[B_i(p), B_j(p)] \qquad (1)$$

where ρ is Spearman's rank correlation of the expression of a single probe, p, across regions in two donors B_i and B_j, and N is the total number of donors. Here, regions correspond to the structural designations provided in the ontology from the AHBA.

The MNI coordinates of tissue samples were updated to those generated via non-linear registration using the Advanced Normalization Tools (ANTs; https://github.com/chrisfilo/alleninf). To increase spatial coverage, tissue samples were mirrored bilaterally across the left and

right hemispheres [122]. Samples were assigned to brain regions in the provided atlas if their MNI coordinates were within 2mm of a given parcel. If a brain region was not assigned a tissue sample based on the above procedure, every voxel in the region was mapped to the nearest tissue sample from the donor in order to generate a dense, interpolated expression map. The average of these expression values was taken across all voxels in the region, weighted by the distance between each voxel and the sample mapped to it, in order to obtain an estimate of the parcellated expression values for the missing region. All tissue samples not assigned to a brain region in the provided atlas were discarded.

Inter-subject variation was addressed by normalizing tissue sample expression values across genes using a robust sigmoid function [52]:

$$x_{\text{norm}} = \frac{1}{1 + \exp(-\frac{(x_g - \langle x_g \rangle)}{\text{IQR}_x})} \quad (2)$$

where $\langle x \rangle$ is the median and IQR_x is the normalized interquartile range of the expression of a single tissue sample across genes. Normalized expression values were then rescaled to the unit interval:

$$x_{\text{scaled}} = \frac{x_{\text{norm}} - \min(x_{\text{norm}})}{\max(x_{\text{norm}}) - \min(x_{\text{norm}})} \quad (3)$$

Gene expression values were then normalized across tissue samples using an identical procedure. Samples assigned to the same brain region were averaged separately for each donor, yielding a regional expression matrix for each donor with 400 rows, corresponding to brain regions, and 15 633 columns, corresponding to the retained genes. A threshold of 0.1 was imposed on the differential stability of each gene, such that only stable genes were retained for future analysis, resulting in 8 687 retained genes.

Finally, the region × region correlated gene expression matrix was constructed by correlating (Pearson's r) the normalized gene expression profile at every pair of brain regions. This matrix was then normalized using Fisher's r-to-z transform.

Receptor similarity

Receptor similarity indexes the degree to which the receptor density profiles at two brain regions are correlated. Conceptually, it can be thought of as how similarly two brain regions might "hear" the same neural signal. PET tracer images for 18 neurotransmitter receptors and transporters were obtained from Hansen et al. [60] and neuromaps (v0.0.1, https://github.com/netneurolab/neuromaps [96]). The receptors/transporters span 9 neurotransmitter systems including: dopamine (D1, D2, DAT), norepinephrine

(NET), serotonin (5-HT1A, 5-HT1B, 5-HT2, 5-HT4, 5-HT6, 5-HTT), acetylcholine ($\alpha_4\beta_2$, M1, VAChT), glutamate (mGluR5), GABA (GABAA), histamine (H3), cannabinoid (CB1), and opioid (MOR). Tracer names and number of participants (with number of females in parentheses) are listed for each receptor in Table S1. Each PET tracer image was parcellated to 400 brain regions and z-scored. A region-by-region receptor similarity matrix was constructed by correlating (Pearson's r) receptor profiles at every pair of brain regions. This matrix was then normalized using Fisher's r-to-z transform.

Laminar similarity

Laminar similarity is estimated from histological data and aims to uncover how similar pairs of brain regions are in terms of cellular distributions across the cortical laminae. Specifically, we use data from the Big-Brain, a high-resolution (20 μm) histological reconstruction of a post-mortem brain from a 65 year old male [4, 112]. Cell-staining intensity profiles were sampled across 50 equivolumetric surfaces from the pial surface to the white mater surface to estimate laminar variation in neuronal density and soma size. Intensity profiles at various cortical depths can be used to approximately identify boundaries of cortical layers that separate supragranular (cortical layers I–III) granular (cortical layer IV), and infragranular (cortical layers V-VI) layers.

The data were obtained on *fsaverage* surface (164k vertices) from the BigBrainWarp toolbox [113] and were parcellated into 400 cortical regions according to the Schaefer-400 atlas [129]. The region × region laminar similarity matrix was calculated as the partial correlation (Pearson's r) of cell intensities between pairs of brain regions, after correcting for the mean intensity across brain regions. Laminar similarity was first introduced in Paquola et al. [112] and has also been referred to as "microstructure profile covariance". This matrix was then normalized using Fisher's r-to-z transform.

Metabolic connectivity

Metabolic connectivity indexes how similarly two brain regions metabolize glucose over time and therefore how similarly two brain regions consume energy. Volumetric 4D PET images of [F^{18}]-fluordoxyglucose (FDG, a glucose analogue) tracer uptake over time were obtained from Jamadar et al. [74]. Specifically, 26 healthy participants (77% female, 18–23 years old) were recruited from the general population and underwent a 95 minute simultaneous MR-PET scan in a Siemens (Erlangen) Biograph 3-Tesla molecular MR scanner. Participants were positioned supine in the scanner bore with their head in a 16-channel radiofrequency head coil and were instructed to lie as still as possible with eyes open and think

of nothing in particular. FDG (average dose 233 MBq) was infused over the course of the scan at a rate of 36 mL/h using a BodyGuard 323 MR-compatible infusion pump (Caesarea Medical Electronics, Caesarea, Israel). Infusion onset was locked to the onset of the PET scan. This data has been validated and analyzed previously in [75, 165].

PET images were reconstructed and preprocessed according to [165]. Specifically, the 5700-second PET time-series for each subject was binned into 356 3D sinogram frames each of 16-second intervals. The attenuation for all required data was corrected via the pseudo-CT method [29]. Ordinary Poisson-Ordered Subset Expectation Maximization algorithm (3 iterations, 21 subsets) with point spread function correction was used to reconstruct 3D volumes from the sinogram frames. The reconstructed DICOM slices were converted to NIFTI format with size $344\times344\times127$ (voxel size: $2.09\times2.09\times2.03$ mm^3) for each volume. A 5 mm FWHM Gaussian postfilter was applied to each 3D volume. All 3D volumes were temporally concatenated to form a 4D ($344\times344\times127\times356$) NIFTI volume. A guided motion correction method using simultaneously acquired MRI was applied to correct the motion during the PET scan. 225 16-second volumes were retained commencing for further analyses.

Next, the 225 PET volumes were motion corrected (FSL MCFLIRT [76]) and the mean PET image was brain extracted and used to mask the 4D data. The fPET data were further processed using a spatiotemporal gradient filter to remove the accumulating effect of the radiotracer and other low-frequency components of the signal [74]. Finally, each time point of the PET volumetric time-series were registered to MNI152 template space using Advanced Normalization Tools in Python (ANTSpy, https://github.com/ANTsX/ANTsPy), parcellated to 400 regions according to the Schaefer atlas, and time-series at pairs of brain regions were correlated (Pearson's r) to construct a metabolic connectivity matrix for each subject. A group-averaged metabolic connectome was obtained by averaging connectivity across subjects, and lastly the matrix was normalized using Fisher's r-to-z transform.

Haemodynamic connectivity

Haemodynamic connectivity, commonly simply referred to as "functional connectivity", captures how similarly pairs of brain regions exhibit fMRI BOLD activity at rest [48]. The fMRI BOLD time-series picks up on magnetic differences between oxygenated and deoxygenated haemoglobin to measure the haemodynamic response: the oversupply of oxygen to active brain regions [82]. Functional magnetic resonance imaging (MRI) data were obtained for 326 unrelated participants (age range 22—35 years, 145 males) from the Human Connectome Project (HCP; S900 release [160]). All four resting state fMRI scans (two scans (R/L and L/R phase encoding directions) on day 1 and two scans (R/L and L/R phase encoding directions) on day 2, each about 15 min long; TR=720 ms) were available for all participants. Functional MRI data were pre-processed using HCP minimal pre-processing pipelines [56, 160]. Specifically, all 3T functional MRI time-series were corrected for gradient nonlinearity, head motion using a rigid body transformation, and geometric distortions using scan pairs with opposite phase encoding directions (R/L, L/R) [37]. Further pre-processing steps include co-registration of the corrected images to the T1w structural MR images, brain extraction, normalization of whole brain intensity, high-pass filtering (>2000s FWHM; to correct for scanner drifts), and removing additional noise using the ICA-FIX process [37, 123]. The pre-processed time-series were then parcellated to 400 cortical brain regions according to the Schaefer atlas [129]. The parcellated time-series were used to construct functional connectivity matrices as a Pearson correlation coefficient between pairs of regional time-series for each of the four scans of each participant. A group-average functional connectivity matrix was constructed as the mean functional connectivity across all individuals and scans. This matrix was then normalized using Fisher's r-to-z transform.

Electrophysiological connectivity

Electrophysiological connectivity was measured using magnetoencephalography (MEG) recordings, which tracks the magnetic field produced by neural currents. Resting state MEG data was acquired for $n = 33$ unrelated healthy young adults (age range 22–35 years) from the Human Connectome Project (S900 release [160]). The data includes resting state scans of approximately 6 minutes long and noise recording for all participants. MEG anatomical data and 3T structural MRI of all participants were also obtained for MEG pre-processing. After preprocessing and parcellating the data, amplitude envelope correlations were performed between time-series at each pair of brain regions, for six canonical frequency bands separately (delta (2–4 Hz), theta (5–7 Hz), alpha (8–12 Hz), beta (15–29 Hz), low gamma (30–59 Hz), and high gamma (60–90 Hz)). Amplitude envelope correlation is applied instead of directly correlating the time-series because of the high sampling rate (2034.5 Hz) of the MEG recordings. The composite electrophysiological connectivity matrix is the first principal component of all six connectivity matrices (vectorized upper triangle), and closely resembles alpha connectivity (Fig. S7). Finally, the matrix underwent Fisher's r-to-z transform. More processing details are described below.

The present MEG data was first processed and used by Shafiei et al. [135]. Resting state MEG data was preprocessed using the open-source software, Brainstorm (https://neuroimage.usc.edu/brainstorm/ [150]), following the online tutorial for the HCP dataset (https://

neuroimage.usc.edu/brainstorm/Tutorials/HCP-MEG). MEG recordings were registered to individual structural MRI images before applying the following preprocessing steps. First, notch filters were applied at 60, 120, 180, 240, and 300 Hz, followed by a high-pass filter at 0.3 Hz to remove slow-wave and DC-offset artifacts. Next, bad channels from artifacts (including heartbeats, eye blinks, saccades, muscle movements, and noisy segments) were removed using Signal-Space Projections (SSP).

Pre-processed sensor-level data was used to construct a source estimation on HCP's fsLR4k cortex surface for each participant. Head models were computed using overlapping spheres and data and noise covariance matrices were estimated from resting state MEG and noise recordings. Linearly constrained minimum variance (LCMV) beamformers was used to obtain the source activity for each participant. Data covariance regularization was performed and the estimated source variance was normalized by the noise covariance matrix to reduce the effect of variable source depth. All eigenvalues smaller than the median eigenvalue of the data covariance matrix were replaced by the median. This helps avoid instability of data covariance inversion caused by the smallest eigenvalues and regularizes the data covariance matrix. Source orientations were constrained to be normal to the cortical surface at each of the $8\,000$ vertex locations on the cortical surface, then parcellated according to the Schaefer-400 atlas [129]. Parcellated time-series were then used to estimate amplitude-based connectivity [27]. An orthogonalization process was applied to correct for the spatial leakage effect by removing all shared zero-lag signals [34].

Temporal profile similarity

Temporal profile similarity was first introduced by, and obtained from, Shafiei et al. [137] and represents how much two brain regions exhibit similar temporal features, as calculated on fMRI time-series. Note that although this connectivity mode is derived from the same imaging modality as haemodynamic connectivity, it is fundamentally different from haemodynamic connectivity as it represents a comprehensive account of dynamic similarity (Pearson's $r = 0.24$, Fig. S3). This is in contrast to haemodynamic connectivity which measures the Pearson's correlation between the time-series themselves. Specifically, we used the highly comparative time-series analysis toolbox, *hctsa* [51, 52] to perform a massive feature extraction of the parcellated fMRI time-series (see *Haemodynamic connectivity*) at each brain region of each participant. The *hctsa* package extracted over $7\,000$ local time-series features using a wide range of operations based on time-series analysis. The extracted features include, but are not limited to, distributional features, entropy and variability, autocorrelation, time-delay embeddings, and nonlinear features of a given time-series. Following the feature extraction procedure, the outputs

of the operations that produced errors were removed and the remaining features ($6\,441$ features) were normalized across nodes using an outlier-robust sigmoidal transform. We used Pearson's correlation coefficients to measure the pairwise similarity between the time-series features of all possible combinations of brain areas. As a result, a temporal profile similarity network was constructed for each individual and each run, representing the strength of the similarity of the local temporal fingerprints of brain areas. This matrix was then normalized using Fisher's r-to-z transform.

Structural connectivity

Diffusion weighted imaging (DWI) data were obtained for 326 unrelated participants (age range 22-35 years, 145 males) from the Human Connectome Project (HCP; S900 release [160]) [37]. DWI data was pre-processed using the MRtrix3 package [153] (https://www.mrtrix. org/). More specifically, fiber orientation distributions were generated using the multi-shell multi-tissue constrained spherical deconvolution algorithm from MRtrix [40, 77]. White matter edges were then reconstructed using probabilistic streamline tractography based on the generated fiber orientation distributions [152]. The tract weights were then optimized by estimating an appropriate cross-section multiplier for each streamline following the procedure proposed by Smith et al. [142] and a connectivity matrix was built for each participant using the 400-region Schaefer parcellation [129]. A group-consensus binary network was constructed using a method that preserves the density and edge-length distributions of the individual connectomes [22, 101, 102]. Edges in the group-consensus network were assigned weights by averaging the log-transformed streamline count of non-zero edges across participants. Edge weights were then scaled to values between 0 and 1.

Disease exposure

Patterns of cortical thickness from the ENIGMA consortium and the *enigma* toolbox were available for thirteen neurological, neurodevelopmental, and psychiatric disorders (https://github.com/MICA-MNI/ENIGMA; [61, 85, 151]), including: 22q11.2 deletion syndrome ($N = 474$ participants, $N = 315$ controls) [148], attention-deficit/hyperactivity disorder (ADHD; $N = 733$ participants, $N = 539$ controls) [71], autism spectrum disorder (ASD; $N = 1571$ participants, $N = 1651$ controls) [161], idiopathic generalized ($N = 367$ participants), right temporal lobe ($N = 339$ participants), and left temporal lobe ($N = 415$ participants) epilepsies ($N = 1727$ controls) [170], depression ($N = 2148$ participants, $N = 7957$ controls) [130], obsessive-compulsive disorder (OCD; $N = 1905$ participants, $N = 1760$ controls) [24], schizophrenia ($N = 4474$ participants, $N = 5098$

controls) [159], bipolar disorder ($N = 1837$ participants, $N = 2582$ controls) [66], obesity ($N = 1223$ participants, $N = 2917$ controls) [111], schizotypy ($N = 3004$ participants) [81], and Parkinson's disease ($N = 2367$ participants, $N = 1183$ controls) [83]. The ENIGMA (Enhancing Neuroimaging Genetics through Meta-Analysis) Consortium is a data-sharing initiative that relies on standardized processing and analysis pipelines, such that disorder maps are comparable [151]. Altogether, over 21 000 participants were scanned across the thirteen disorders, against almost 26 000 controls. The analysis was limited to adults in all cases except ASD where the cortical abnormality map is only available aggregated across all ages (2–64 years). The values for each map are z-scored effect sizes (Cohen's d) of cortical thickness in patient populations versus healthy controls. Imaging and processing protocols can be found at http://enigma.ini. usc.edu/protocols/. Local review boards and ethics committees approved each individual study separately, and written informed consent was provided according to local requirements.

We calculate disease exposure for every disease and network, after masking the network such that all edges with negative strength are assigned a strength of 0. For a given network and disease, disease exposure of a node i is defined as,

$$D_i = \frac{1}{N_i} \sum_{j \neq i, j=1}^{N_i} d_j \times c_{ij} \tag{4}$$

where N_i is the number of positive connections made by region i, d_j is the cortical abnormality at region j, and c_{ij} is the edge strength between regions i and j. This analysis was repeated after regressing the exponential fit in Fig. 1b from each network, to ensure results are not driven by distance (Fig. S6).

Community detection

For each connectivity mode, communities were identified using the Louvain algorithm, which maximizes positive edge strength within communities and negative edge strength between communities [23]. Specifically, brain regions were assigned to communities in a manner that maximizes the quality function

$$Q(\gamma) = \frac{1}{m^+} [w_{ij}^+ - \gamma p_{ij}^+] \delta(\sigma_i, \sigma_j)$$
$$- \frac{1}{m^+ + m^-} \sum_{ij} [w_{ij}^+ - \delta p_{ij}^-] \delta(\sigma_i, \sigma_j) \tag{5}$$

where w_{ij}^+ is the network with only positive correlations and likewise for w_{ij}^- and negative correlations. The term $p_{ij}^\pm = (s_i^\pm s_j^\pm)/(2m^\pm)$ represents the null model: the expected density of connections between nodes i and j,

where $s_i^\pm = \sum_j w_{ij}^\pm$ and $m^\pm = \sum_{i,j>i} w_{ij}^\pm$. The variable σ_i is the community assignment of node i and $\delta(\sigma_i, \sigma_j)$ is the Kronecker function and is equal to 1 when $\sigma_i = \sigma_j$ and 0 otherwise. The resolution parameter, γ, scales the relative importance of the null model, making it easier ($\gamma > 1$) or harder ($\gamma < 1$) for the algorithm to uncover many communities. In other words, as γ increases, increasingly fine network partitions are identified. We tested 60 values of γ, from $\gamma = 0.1$ to $\gamma = 6.0$, in increments of 0.1. At each γ, we repeated the algorithm 250 times and constructed a consensus partition, following the procedure recommended in Bassett et al. [12].

Similarity network fusion

First introduced by Wang et al. [168], similarity network fusion (SNF) is a method for combining multiple measurement types for the same observations (e.g. patients, or in our case, brain regions) into a single similarity network where edges between observations represent their cross-modal similarity. For each data source, SNF constructs an independent similarity network, defines the K nearest neighbours for each observation, then iteratively combines the networks in a manner that gives more weight to edges between observations that are consistently high-strength across data types. We used snfpy (https://github.com/rmarkello/snfpy [98]), an open-source Python implementation of the original SNF code provied by Wang et al. [168]. A brief description of the main steps in SNF follows, adapted from its original presentation in Wang et al. [168].

In the present report, the seven data sources to be fused are the seven connectivity modes (correlated gene expression, receptor similarity, laminar similarity, metabolic connectivity, haemodynamic connectivity, electrophysiological connectivity, and temporal similarity). First, similarity networks for each connectivity mode is constructed where edges are determined using a scaled exponential similarity kernel:

$$\mathbf{W}(i,j) = e^{-\frac{\rho^2(x_i, x_j)}{\mu \epsilon_{i,j}}} \tag{6}$$

where $\mathbf{W}(i,j)$ is the edge weight between regions i and j, $\rho(x_i, x_j)$ is the Euclidean distance between regions i and j, $\mu \in \mathbb{R}$ is a hyperparameter that is set empirically, and

$$\epsilon_{i,j} = \frac{\bar{\rho}(x_i, N_i) + \bar{\rho}(x_j, N_j) + \rho(x_i, x_j)}{3} \tag{7}$$

where $\bar{\rho}(x_i, N_i)$ is the average distance between x_i and all other regions in the network. Note that μ is a scaling factor that determines the weighting of edges between regions in the similarity network, and is set to $\mu = 0.5$ in the present report.

Next, each $\mathbf{W}$ is normalized such that:

$$\mathbf{P}(i,j) = \begin{cases} \frac{W(i,j)}{2\sum_{k\neq i} W(i,k)}, & j \neq i \\ \frac{1}{2}, & j = 1 \end{cases} \quad (8)$$

Finally, a sparse matrix $\mathbf{S}$ of the K nearest (i.e. strongest) neighbours is constructed:

$$\mathbf{S}(i,j) = \begin{cases} \frac{W(i,j)}{\sum_{k\in N_i} W(i,k)}, & j \in N_i \\ 0, & \text{otherwise} \end{cases} \quad (9)$$

In other words, the matrix $\mathbf{P}$ encodes the full information about the similarity of each region to all other regions (within a given connectivity mode), whereas $\mathbf{S}$ encodes only the similarity of the K most similar regions to each region. K is SNF's second hyperparameter, which we set to one tenth the number of regions in the network (40).

The similarity networks are then iteratively fused. At each iteration, the matrices are made more similar to each other via:

$$\mathbf{P}^{(v)} = \mathbf{S}^{(v)} \times \frac{\sum_{k\neq v} \mathbf{P}^{(k)}}{m-1} \times (\mathbf{S}^{(v)})^{\mathrm{T}}, v = \{1,2,\dots m\} \quad (10)$$

After each iteration, the generated matrices are renormalized as in Equation 8. Fusion stops when the matrices have converged or after a specified number of iterations (in our case, 20). Regions x_i and x_j will likely be neighbours in the fused network if they are neighbours in multiple similarity networks. Furthermore, if x_i and x_j are not very similar in one data type, their similarity can be expressed in another data type.

After the fusion process, we confirm that no single network exerts undue influence on the final fused network by repeating the fusion process while excluding a single network. The minimum correlation (Spearman r) between the leave-one-out fused network and the complete fused network is 0.958. In addition to this, we confirm that alternative K and μ parameters would not make large difference to the fused network. We test $K \in [20, 59]$ and $\mu \in [0.3, 0.8]$ and find that these alternative fused networks are highly correlated with the original (minimum Spearman $r = 0.924$).

Null models

Spin tests Spatial autocorrelation-preserving permutation tests were used to assess statistical significance of associations across brain regions, termed "spin tests" [3, 97, 162]. We created a surface-based representation of the parcellation on the FreeSurfer fsaverage surface, via files from the Connectome Mapper toolkit (https://github.com/LTS5/cmp). We used the spherical projection of the fsaverage surface to define spatial coordinates for each parcel by selecting the coordinates of

the vertex closest to the center of the mass of each parcel [163]. These parcel coordinates were then randomly rotated, and original parcels were reassigned the value of the closest rotated parcel (10 000 repetitions). Parcels for which the medial wall was closest were assigned the value of the next most proximal parcel instead. The procedure was performed at the parcel resolution rather than the vertex resolution to avoid upsampling the data, and to each hemisphere separately.

Network randomization Structural networks were randomized using a procedure that preserves the density, edge length, degree distributions of the empirical network [21, 162]. Edges were binned according to Euclidean distance (10 bins). Within each bin, pairs of edges were selected at random and swapped, for a total number of swaps equal to the number of regions in the network multiplied by 20. This procedure was repeated 1 000 times to generate 1 000 null structural networks, which were then used to generate null distributions of network-level measures.

Code and data availability

All code and data used to perform the analyses are available at https://github.com/netneurolab/hansen_many_networks.

Competing interests

The authors declare no competing interests.

Acknowledgements

[1] Aertsen, A., Gerstein, G., Habib, M., and Palm, G. (1989). Dynamics of neuronal firing correlation: modulation of" effective connectivity". *Journal of neurophysiology*, 61(5):900–917.

[2] Aghourian, M., Legault-Denis, C., Soucy, J., Rosa-Neto, P., Gauthier, S., Kostikov, A., Gravel, P., and Bedard, M. (2017). Quantification of brain cholinergic denervation in alzheimer's disease using pet imaging with [18 f]-feobv. *Molecular psychiatry*, 22(11):1531–1538.

[3] Alexander-Bloch, A. F., Shou, H., Liu, S., Satterthwaite, T. D., Glahn, D. C., Shinohara, R. T., Vandekar, S. N., and Raznahan, A. (2018). On testing for spatial correspondence between maps of human brain structure and function. *NeuroImage*, 178:540–551.

[4] Amunts, K., Lepage, C., Borgeat, L., Mohlberg, H., Dickscheid, T., Rousseau, M.-É., Bludau, S., Bazin, P.-L., Lewis, L. B., Oros-Peusquens, A.-M., et al. (2013). Bigbrain: an ultrahigh-resolution 3d human brain model. *Science*, 340(6139):1472–1475.

[5] Arnatkeviciute, A., Fulcher, B. D., Oldham, S., Tiego, J., Paquola, C., Gerring, Z., Aquino, K., Hawi, Z., Johnson, B., Ball, G., et al. (2021). Genetic influences on hub connectivity of the human connectome. *Nature Communications*, 12(1):1–14.

[6] Arnatkevičiūtė, A., Fulcher, B. D., and Fornito, A. (2019). A practical guide to linking brain-wide gene expression and neuroimaging data. *Neuroimage*, 189:353–367.

[7] Assaf, Y., Blumenfeld-Katzir, T., Yovel, Y., and Basser, P. J. (2008). Axcaliber: a method for measuring axon diameter distribution from diffusion mri. *Magnetic Resonance in Medicine: An Official Journal of the International Society for Magnetic Resonance in Medicine*, 59(6):1347–1354.

[8] Avena-Koenigsberger, A., Misic, B., and Sporns, O. (2018). Communication dynamics in complex brain networks. *Nature Reviews Neuroscience*, 19(1):17–33.

[9] Baldassarri, S. R., Hillmer, A. T., Anderson, J. M., Jatlow, P., Nabulsi, N., Labaree, D., Cosgrove, K. P., O'Malley, S. S., Eissenberg, T., Krishnan-Sarin, S., et al. (2018). Use of electronic cigarettes leads to significant beta2-nicotinic acetylcholine receptor occupancy: evidence from a pet imaging study. *Nicotine and Tobacco Research*, 20(4):425–433.

[10] Baldassarri, S. R., Park, E., Finnema, S. J., Planeta, B., Nabulsi, N., Najafzadeh, S., Ropchan, J., Huang, Y., Hannestad, J., Maloney, K., et al. (2020). Inverse changes in raphe and cortical 5-ht1b receptor availability after acute tryptophan depletion in healthy human subjects. *Synapse*, 74(10):e22159.

[11] Baldermann, J. C., Schüller, T., Kohl, S., Voon, V., Li, N., Hollunder, B., Figee, M., Haber, S. N., Sheth, S. A., Mosley, P. E., et al. (2021). Connectomic deep brain stimulation for obsessive-compulsive disorder. *Biological Psychiatry*, 90(10):678–688.

[12] Bassett, D. S., Porter, M. A., Wymbs, N. F., Grafton, S. T., Carlson, J. M., and Mucha, P. J. (2013). Robust detection of dynamic community structure in networks. *Chaos: An Interdisciplinary Journal of Nonlinear Science*, 23(1):013142.

[13] Bassett, D. S. and Sporns, O. (2017). Network neuroscience. *Nature neuroscience*, 20(3):353–364.

[14] Baum, G. L., Cui, Z., Roalf, D. R., Ciric, R., Betzel, R. F., Larsen, B., Cieslak, M., Cook, P. A., Xia, C. H., Moore, T. M., et al. (2020). Development of structure–function coupling in human brain networks during youth. *Proceedings of the National Academy of Sciences*, 117(1):771–778.

[15] Bazinet, V., de Wael, R. V., Hagmann, P., Bernhardt, B. C., and Misic, B. (2021). Multiscale communication in cortico-cortical networks. *NeuroImage*, 243:118546.

[16] Bazinet, V., Hansen, J. Y., de Wael, R. V., Bernhardt, B. C., van den Heuvel, M. P., and Misic, B. (2022). Assortative mixing in micro-architecturally annotated brain connectomes. *bioRxiv*.

[17] Bedard, M.-A., Aghourian, M., Legault-Denis, C., Postuma, R. B., Soucy, J.-P., Gagnon, J.-F., Pelletier, A., and Montplaisir, J. (2019). Brain cholinergic alterations in idiopathic rem sleep behaviour disorder: a pet imaging study with 18f-feobv. *Sleep medicine*, 58:35–41.

[18] Belfort-DeAguiar, R., Gallezot, J.-D., Hwang, J. J., Elshafie, A., Yeckel, C. W., Chan, O., Carson, R. E., Ding, Y.-S., and Sherwin, R. S. (2018). Noradrenergic activity in the human brain: a mechanism supporting the defense against hypoglycemia. *The Journal of Clinical Endocrinology & Metabolism*, 103(6):2244–2252.

[19] Beliveau, V., Ganz, M., Feng, L., Ozenne, B., Højgaard, L., Fisher, P. M., Svarer, C., Greve, D. N., and Knudsen, G. M. (2017). A high-resolution in vivo atlas of the human brain's serotonin system. *Journal of Neuroscience*, 37(1):120–128.

[20] Bernhardt, B. C., Smallwood, J., Keilholz, S., and Margulies, D. S. (2022). Gradients in brain organization. *NeuroImage*, 251:118987.

[21] Betzel, R. F. and Bassett, D. S. (2018). Specificity and robustness of long-distance connections in weighted, interareal connectomes. *Proceedings of the National Academy of Sciences*, 115(21):E4880–E4889.

[22] Betzel, R. F., Griffa, A., Hagmann, P., and Mišić, B. (2019). Distance-dependent consensus thresholds for generating group-representative structural brain networks. *Network neuroscience*, 3(2):475–496.

[23] Blondel, V. D., Guillaume, J.-L., Lambiotte, R., and Lefebvre, E. (2008). Fast unfolding of communities in large networks. *Journal of statistical mechanics: theory and experiment*, 2008(10):P10008.

[24] Boedhoe, P. S., Schmaal, L., Abe, Y., Alonso, P., Ameis, S. H., Anticevic, A., Arnold, P. D., Batistuzzo, M. C., Benedetti, F., Beucke, J. C., et al. (2018). Cortical abnormalities associated with pediatric and adult obsessive-compulsive disorder: findings from the enigma obsessive-compulsive disorder working group. *American Journal of Psychiatry*, 175(5):453–462.

[25] Brookes, M. J., Hale, J. R., Zumer, J. M., Stevenson, C. M., Francis, S. T., Barnes, G. R., Owen, J. P., Morris, P. G., and Nagarajan, S. S. (2011a). Measuring functional connectivity using meg: methodology and comparison with fcmri. *Neuroimage*, 56(3):1082–1104.

[26] Brookes, M. J., Woolrich, M., Luckhoo, H., Price, D., Hale, J. R., Stephenson, M. C., Barnes, G. R., Smith, S. M., and Morris, P. G. (2011b). Investigating the elec-

trophysiological basis of resting state networks using magnetoencephalography. *Proceedings of the National Academy of Sciences*, 108(40):16783–16788.

[27] Bruns, A., Eckhorn, R., Jokeit, H., and Ebner, A. (2000). Amplitude envelope correlation detects coupling among incoherent brain signals. *Neuroreport*, 11(7):1509–1514.

[28] Bullmore, E. and Sporns, O. (2012). The economy of brain network organization. *Nature reviews neuroscience*, 13(5):336–349.

[29] Burgos, N., Cardoso, M. J., Thielemans, K., Modat, M., Pedemonte, S., Dickson, J., Barnes, A., Ahmed, R., Mahoney, C. J., Schott, J. M., et al. (2014). Attenuation correction synthesis for hybrid pet-mr scanners: application to brain studies. *IEEE transactions on medical imaging*, 33(12):2332–2341.

[30] Cammoun, L., Gigandet, X., Meskaldji, D., Thiran, J. P., Sporns, O., Do, K. Q., Maeder, P., Meuli, R., and Hagmann, P. (2012). Mapping the human connectome at multiple scales with diffusion spectrum mri. *J Neurosci Meth*, 203(2):386–397.

[31] Chiang-shan, R. L., Potenza, M. N., Lee, D. E., Planeta, B., Gallezot, J.-D., Labaree, D., Henry, S., Nabulsi, N., Sinha, R., Ding, Y.-S., et al. (2014). Decreased norepinephrine transporter availability in obesity: positron emission tomography imaging with (s, s)-[11c] o-methylreboxetine. *Neuroimage*, 86:306–310.

[32] Chopra, S., Oldham, S., Segal, A., Holmes, A., Sabaroedin, K., Orchard, E. R., Francey, S. M., ODonoghue, B., Cropley, V., Nelson, B., et al. (2022). Network constraints on longitudinal grey matter changes in first episode psychosis. *medRxiv*.

[33] Chu, C. J., Tanaka, N., Diaz, J., Edlow, B. L., Wu, O., Hämäläinen, M., Stufflebeam, S., Cash, S. S., and Kramer, M. A. (2015). Eeg functional connectivity is partially predicted by underlying white matter connectivity. *Neuroimage*, 108:23–33.

[34] Colclough, G. L., Woolrich, M. W., Tewarie, P., Brookes, M. J., Quinn, A. J., and Smith, S. M. (2016). How reliable are meg resting-state connectivity metrics? *Neuroimage*, 138:284–293.

[35] Colizza, V., Flammini, A., Serrano, M. A., and Vespignani, A. (2006). Detecting rich-club ordering in complex networks. *Nature physics*, 2(2):110–115.

[36] Collin, G., Sporns, O., Mandl, R. C., and Van Den Heuvel, M. P. (2014). Structural and functional aspects relating to cost and benefit of rich club organization in the human cerebral cortex. *Cerebral cortex*, 24(9):2258–2267.

[37] de Wael, R. V., Larivière, S., Caldairou, B., Hong, S.-J., Margulies, D. S., Jefferies, E., Bernasconi, A., Smallwood, J., Bernasconi, N., and Bernhardt, B. C. (2018). Anatomical and microstructural determinants of hippocampal subfield functional connectome embedding. *Proceedings of the National Academy of Sciences*, 115(40):10154–10159.

[38] Dear, R., Seidlitz, J., Markello, R. D., Arnatkeviciute, A., Anderson, K. M., Bethlehem, R. A., Wagstyl, K., Bullmore, E. T., Raznahan, A., Vertes, P., et al. (2022). Three transcriptional axes underpin anatomy, development, and disorders of the human cortex. *bioRxiv*.

[39] Desikan, R. S., Ségonne, F., Fischl, B., Quinn, B. T., Dickerson, B. C., Blacker, D., Buckner, R. L., Dale, A. M., Maguire, R. P., Hyman, B. T., et al. (2006). An automated labeling system for subdividing the human cerebral cortex on mri scans into gyral based regions of interest. *NeuroImage*, 31(3):968–980.

[40] Dhollander, T., Raffelt, D., and Connelly, A. (2016). Unsupervised 3-tissue response function estimation from single-shell or multi-shell diffusion mr data without a co-registered t1 image. In *ISMRM Workshop on Breaking the Barriers of Diffusion MRI*, volume 5. ISMRM.

[41] Ding, Y.-S., Singhal, T., Planeta-Wilson, B., Gallezot, J.-D., Nabulsi, N., Labaree, D., Ropchan, J., Henry, S., Williams, W., Carson, R. E., et al. (2010). Pet imaging of the effects of age and cocaine on the norepinephrine transporter in the human brain using (s, s)-[11c] o-methylreboxetine and hrrt. *Synapse*, 64(1):30–38.

[42] Dipasquale, O., Selvaggi, P., Veronese, M., Gabay, A. S., Turkheimer, F., and Mehta, M. A. (2019). Receptor-enriched analysis of functional connectivity by targets (react): A novel, multimodal analytical approach informed by pet to study the pharmacodynamic response of the brain under mdma. *Neuroimage*, 195:252–260.

[43] DuBois, J. M., Rousset, O. G., Rowley, J., Porras-Betancourt, M., Reader, A. J., Labbe, A., Massarweh, G., Soucy, J.-P., Rosa-Neto, P., and Kobayashi, E. (2016). Characterization of age/sex and the regional distribution of mglur5 availability in the healthy human brain measured by high-resolution [11 c] abp688 pet. *European journal of nuclear medicine and molecular imaging*, 43(1):152–162.

[44] Dukart, J., Holiga, Š., Chatham, C., Hawkins, P., Forsyth, A., McMillan, R., Myers, J., Lingford-Hughes, A. R., Nutt, D. J., Merlo-Pich, E., et al. (2018). Cerebral blood flow predicts differential neurotransmitter activity. *Scientific reports*, 8(1):1–11.

[45] D'Souza, D. C., Cortes-Briones, J. A., Ranganathan, M., Thurnauer, H., Creatura, G., Surti, T., Planeta, B., Neumeister, A., Pittman, B., Normandin, M. D., et al. (2016). Rapid changes in cannabinoid 1 receptor availability in cannabis-dependent male subjects after abstinence from cannabis. *Biological psychiatry: cognitive neuroscience and neuroimaging*, 1(1):60–67.

[46] Ekelund, J., Slifstein, M., Narendran, R., Guillin, O., Belani, H., Guo, N.-N., Hwang, Y., Hwang, D.-R., Abi-Dargham, A., and Laruelle, M. (2007). In vivo da d 1 receptor selectivity of nnc 112 and sch 23390. *Molecular imaging and biology*, 9(3):117–125.

[47] Fornito, A., Arnatkevičiūtė, A., and Fulcher, B. D. (2019). Bridging the gap between connectome and transcriptome. *Trends in Cognitive Sciences*, 23(1):34–50.

[48] Fox, M. D. and Raichle, M. E. (2007). Spontaneous fluctuations in brain activity observed with functional magnetic resonance imaging. *Nature reviews neuroscience*, 8(9):700–711.

[49] Friston, K. J. (2011). Functional and effective connectivity: a review. *Brain connectivity*, 1(1):13–36.

[50] Fulcher, B. D. and Fornito, A. (2016). A transcriptional signature of hub connectivity in the mouse connectome. *Proc Natl Acad Sci USA*, 113(5):1435–1440.

[51] Fulcher, B. D. and Jones, N. S. (2017). hctsa: A computational framework for automated time-series phenotyping using massive feature extraction. *Cell systems*, 5(5):527–531.

[52] Fulcher, B. D., Little, M. A., and Jones, N. S. (2013). Highly comparative time-series analysis: the empirical structure of time series and their methods. *Journal of the Royal Society Interface*, 10(83):20130048.

[53] Gallezot, J.-D., Nabulsi, N., Neumeister, A., Planeta-Wilson, B., Williams, W. A., Singhal, T., Kim, S., Maguire, R. P., McCarthy, T., Frost, J. J., et al. (2010). Kinetic modeling of the serotonin 5-ht1b receptor radioligand [11c] p943 in humans. *Journal of Cerebral Blood Flow & Metabolism*, 30(1):196–210.

[54] Gallezot, J.-D., Planeta, B., Nabulsi, N., Palumbo, D., Li, X., Liu, J., Rowinski, C., Chidsey, K., Labaree, D., Ropchan, J., et al. (2017). Determination of receptor occupancy in the presence of mass dose:[11c] gsk189254 pet imaging of histamine h3 receptor occupancy by pf-03654746. *Journal of Cerebral Blood Flow & Metabolism*, 37(3):1095–1107.

[55] Garces, P., Pereda, E., Hernández-Tamames, J. A., Del-Pozo, F., Maestu, F., and Ángel Pineda-Pardo, J. (2016). Multimodal description of whole brain connectivity: A comparison of resting state meg, fmri, and dwi. *Human brain mapping*, 37(1):20–34.

[56] Glasser, M. F., Sotiropoulos, S. N., Wilson, J. A., Coalson, T. S., Fischl, B., Andersson, J. L., Xu, J., Jbabdi, S., Webster, M., Polimeni, J. R., et al. (2013). The minimal preprocessing pipelines for the human connectome project. *Neuroimage*, 80:105–124.

[57] Griffa, A. and Van den Heuvel, M. P. (2018). Rich-club neurocircuitry: function, evolution, and vulnerability. *Dialogues in clinical neuroscience*.

[58] Hagmann, P., Cammoun, L., Gigandet, X., Meuli, R., Honey, C. J., Wedeen, V. J., and Sporns, O. (2008). Mapping the structural core of human cerebral cortex. *PLoS biology*, 6(7):e159.

[59] Hänisch, B., Hansen, J. Y., Bernhardt, B. C., Eickhoff, S. B., Dukart, J., Misic, B., and Valk, S. L. (2022). Neurotransmitter transporter/receptor co-expression shares organizational traits with brain structure and function. *bioRxiv*.

[60] Hansen, J. Y., Shafiei, G., Markello, R. D., Smart, K., Cox, S. M., Nørgaard, M., Beliveau, V., Wu, Y., Gallezot, J.-D., Aumont, É., et al. (2022a). Mapping neurotransmitter systems to the structural and functional organization of the human neocortex. *Nature Neuroscience*, pages 1–13.

[61] Hansen, J. Y., Shafiei, G., Vogel, J. W., Smart, K., Bearden, C. E., Hoogman, M., Franke, B., Van Rooij, D., Buitelaar, J., McDonald, C. R., et al. (2022b). Local molecular and global connectomic contributions to cross-disorder cortical abnormalities. *Nature communications*, 13(1):1–17.

[62] Hawrylycz, M., Miller, J. A., Menon, V., Feng, D., Dolbeare, T., Guillozet-Bongaarts, A. L., Jegga, A. G., Aronow, B. J., Lee, C.-K., Bernard, A., et al. (2015). Canonical genetic signatures of the adult human brain. *Nat Neurosci*, 18(12):1832.

[63] Hawrylycz, M. J., Lein, E. S., Guillozet-Bongaarts, A. L., Shen, E. H., Ng, L., Miller, J. A., Van De Lagemaat, L. N., Smith, K. A., Ebbert, A., Riley, Z. L., et al. (2012). An anatomically comprehensive atlas of the adult human brain transcriptome. *Nature*, 489(7416):391.

[64] He, B. J., Snyder, A. Z., Zempel, J. M., Smyth, M. D., and Raichle, M. E. (2008). Electrophysiological correlates of the brain's intrinsic large-scale functional architecture. *Proceedings of the National Academy of Sciences*, 105(41):16039–16044.

[65] Hettwer, M., Larivière, S., Park, B., van den Heuvel, O., Schmaal, L., Andreassen, O., Ching, C., Hoogman, M., Buitelaar, J., van Rooij, D., et al. (2022). Coordinated cortical thickness alterations across six neurodevelopmental and psychiatric disorders. *Nature Communications*, 13(1):1–14.

[66] Hibar, D., Westlye, L. T., Doan, N. T., Jahanshad, N., Cheung, J., Ching, C. R., Versace, A., Bilderbeck, A., Uhlmann, A., Mwangi, B., et al. (2018). Cortical abnormalities in bipolar disorder: an mri analysis of 6503 individuals from the enigma bipolar disorder working group. *Molecular psychiatry*, 23(4):932–942.

[67] Hilgetag, C. C., Beul, S. F., van Albada, S. J., and Goulas, A. (2019). An architectonic type principle integrates macroscopic cortico-cortical connections with intrinsic cortical circuits of the primate brain. *Network neuroscience*, 3(4):905–923.

[68] Hill, J., Inder, T., Neil, J., Dierker, D., Harwell, J., and Van Essen, D. (2010). Similar patterns of cortical expansion during human development and evolution. *Proceedings of the National Academy of Sciences*, 107(29):13135–13140.

[69] Hillmer, A. T., Esterlis, I., Gallezot, J.-D., Bois, F., Zheng, M.-Q., Nabulsi, N., Lin, S.-F., Papke, R., Huang, Y., Sabri, O., et al. (2016). Imaging of cerebral $\alpha 4\beta 2^*$ nicotinic acetylcholine receptors with (-)-[18f] flubatine pet: Implementation of bolus plus constant infusion and sensitivity to acetylcholine in human brain. *Neuroimage*, 141:71–80.

[70] Honey, C. J., Sporns, O., Cammoun, L., Gigandet, X., Thiran, J.-P., Meuli, R., and Hagmann, P. (2009). Predicting human resting-state functional connectivity from structural connectivity. *Proceedings of the National Academy of Sciences*, 106(6):2035–2040.

[71] Hoogman, M., Muetzel, R., Guimaraes, J. P., Shumskaya, E., Mennes, M., Zwiers, M. P., Jahanshad, N., Sudre, G., Wolfers, T., Earl, E. A., et al. (2019). Brain imaging of the cortex in adhd: a coordinated analysis of large-scale clinical and population-based samples. *American Journal of Psychiatry*, 176(7):531–542.

[72] Horn, A., Reich, M., Vorwerk, J., Li, N., Wenzel, G., Fang, Q., Schmitz-Hübsch, T., Nickl, R., Kupsch, A., Volkmann, J., et al. (2017). Connectivity predicts deep brain stimulation outcome in p arkinson disease. *Annals of neurology*, 82(1):67–78.

[73] Huntenburg, J. M., Bazin, P.-L., and Margulies, D. S. (2018). Large-scale gradients in human cortical organization. *Trends Cogn Sci*, 22(1):21–31.

[74] Jamadar, S. D., Ward, P. G., Close, T. G., Fornito, A., Premaratne, M., O'Brien, K., Stäb, D., Chen, Z., Shah, N. J., and Egan, G. F. (2020). Simultaneous bold-fmri and constant infusion fdg-pet data of the resting human brain. *Scientific data*, 7(1):1–12.

[75] Jamadar, S. D., Ward, P. G., Liang, E. X., Orchard, E. R., Chen, Z., and Egan, G. F. (2021). Metabolic and hemodynamic resting-state connectivity of the human brain: a high-temporal resolution simultaneous bold-fmri and fdg-fpet multimodality study. *Cerebral Cortex*, 31(6):2855–2867.

[76] Jenkinson, M., Bannister, P., Brady, M., and Smith, S. (2002). Improved optimization for the robust and accurate linear registration and motion correction of brain images. *Neuroimage*, 17(2):825–841.

[77] Jeurissen, B., Tournier, J.-D., Dhollander, T., Connelly, A., and Sijbers, J. (2014). Multi-tissue constrained spherical deconvolution for improved analysis of multi-shell diffusion mri data. *NeuroImage*, 103:411–426.

[78] Jones, D. K., Knösche, T. R., and Turner, R. (2013). White matter integrity, fiber count, and other fallacies: the do's and don'ts of diffusion mri. *Neuroimage*, 73:239–254.

[79] Kaller, S., Rullmann, M., Patt, M., Becker, G.-A., Luthardt, J., Girbardt, J., Meyer, P. M., Werner, P., Barthel, H., Bresch, A., et al. (2017). Test–retest measurements of dopamine d 1-type receptors using simultaneous pet/mri imaging. *European journal of nuclear medicine and molecular imaging*, 44(6):1025–1032.

[80] Kantonen, T., Karjalainen, T., Isojärvi, J., Nuutila, P., Tuisku, J., Rinne, J., Hietala, J., Kaasinen, V., Kalliokoski, K., Scheinin, H., et al. (2020). Interindividual variability and lateralization of μ-opioid receptors in the human brain. *NeuroImage*, 217:116922.

[81] Kirschner, M., Hodzic-Santor, B., Antoniades, M., Nenadic, I., Kircher, T., Krug, A., Meller, T., Grotegerd, D., Fornito, A., Arnatkeviciute, A., et al. (2022). Cortical and subcortical neuroanatomical signatures of schizotypy in 3004 individuals assessed in a worldwide enigma study. *Molecular psychiatry*, 27(2):1167–1176.

[82] Kwong, K. K., Belliveau, J. W., Chesler, D. A., Goldberg, I. E., Weisskoff, R. M., Poncelet, B. P., Kennedy, D. N., Hoppel, B. E., Cohen, M. S., and Turner, R. (1992). Dynamic magnetic resonance imaging of human brain activity during primary sensory stimulation. *Proceedings of the National Academy of Sciences*, 89(12):5675–5679.

[83] Laansma, M. A., Bright, J. K., Al-Bachari, S., Anderson, T. J., Ard, T., Assogna, F., Baquero, K. A., Berendse, H. W., Blair, J., Cendes, F., et al. (2021). International multicenter analysis of brain structure across clinical stages of parkinson's disease. *Movement Disorders*.

[84] Lanciego, J. L. and Wouterlood, F. G. (2020). Neuroanatomical tract-tracing techniques that did go viral. *Brain Structure and Function*, 225(4):1193–1224.

[85] Larivière, S., Paquola, C., Park, B.-y., Royer, J., Wang, Y., Benkarim, O., Vos de Wael, R., Valk, S. L., Thomopoulos, S. I., Kirschner, M., et al. (2021). The enigma toolbox: multiscale neural contextualization of multisite neuroimaging datasets. *Nature Methods*, 18(7):698–700.

[86] Lawn, T., Howarda, M. A., Turkheimera, F., Misicb, B., Decoc, G., Martinsa, D., and Dipasqualea, O. (2022). From neurotransmitters to networks: Transcending organisational hierarchies with molecular-informed functional imaging. *PsyArXiv*.

[87] Liang, X., Zou, Q., He, Y., and Yang, Y. (2013). Coupling of functional connectivity and regional cerebral blood flow reveals a physiological basis for network hubs of the human brain. *Proceedings of the National Academy of Sciences*, 110(5):1929–1934.

[88] Lichtman, J. W. and Denk, W. (2011). The big and the small: challenges of imaging the brain's circuits. *Science*, 334(6056):618–623.

[89] Lichtman, J. W., Livet, J., and Sanes, J. R. (2008). A technicolour approach to the connectome. *Nature Reviews Neuroscience*, 9(6):417–422.

[90] Lutti, A., Dick, F., Sereno, M. I., and Weiskopf, N. (2014). Using high-resolution quantitative mapping of r1 as an index of cortical myelination. *Neuroimage*, 93:176–188.

[91] Maier-Hein, K. H., Neher, P. F., Houde, J.-C., Côté, M.-A., Garyfallidis, E., Zhong, J., Chamberland, M., Yeh, F.-C., Lin, Y.-C., Ji, Q., et al. (2017). The challenge of mapping the human connectome based on diffusion tractography. *Nature communications*, 8(1):1–13.

[92] Mancuso, L., Uddin, L. Q., Nani, A., Costa, T., and Cauda, F. (2019). Brain functional connectivity in individuals with callosotomy and agenesis of the corpus callosum: A systematic review. *Neuroscience & Biobehavioral Reviews*, 105:231–248.

[93] Mansour, S., Seguin, C., Winkler, A., Noble, S., and Zalesky, A. (2022). Topological cluster statistic (tcs): Towards structural-connectivity-guided fmri cluster enhancement. *Research Square*.

[94] Margulies, D. S., Ghosh, S. S., Goulas, A., Falkiewicz, M., Huntenburg, J. M., Langs, G., Bezgin, G., Eickhoff, S. B., Castellanos, F. X., Petrides, M., et al. (2016). Situating the default-mode network along a principal gradient of macroscale cortical organization. *Proc Natl Acad Sci USA*, 113(44):12574–12579.

[95] Markello, R. D., Arnatkeviciute, A., Poline, J.-B., Fulcher, B. D., Fornito, A., and Misic, B. (2021a). Standardizing workflows in imaging transcriptomics with the abagen toolbox. *Elife*, 10:e72129.

[96] Markello, R. D., Hansen, J. Y., Liu, Z.-Q., Bazinet, V., Shafiei, G., Suárez, L. E., Blostein, N., Seidlitz, J., Baillet, S., Satterthwaite, T. D., et al. (2022). Neuromaps: structural and functional interpretation of brain maps. *Nature Methods*, pages 1–8.

[97] Markello, R. D. and Misic, B. (2021). Comparing spatial null models for brain maps. *NeuroImage*, page 118052.

[98] Markello, R. D., Shafiei, G., Tremblay, C., Postuma, R. B., Dagher, A., and Misic, B. (2021b). Multimodal phenotypic axes of parkinson's disease. *npj Parkinson's Disease*, 7(1):1–12.

[99] Matuskey, D., Bhagwagar, Z., Planeta, B., Pittman, B., Gallezot, J.-D., Chen, J., Wanyiri, J., Najafzadeh, S., Ropchan, J., Geha, P., et al. (2014). Reductions in brain 5-ht1b receptor availability in primarily cocaine-dependent humans. *Biological psychiatry*, 76(10):816–822.

[100] Mills, B. D., Grayson, D. S., Shunmugavel, A., Miranda-Dominguez, O., Feczko, E., Earl, E., Neve, K. A., and Fair, D. A. (2018). Correlated gene expression and anatomical communication support synchronized brain activity in the mouse functional connectome. *Journal of Neuroscience*, 38(25):5774–5787.

[101] Mišić, B., Betzel, R. F., Griffa, A., De Reus, M. A., He, Y., Zuo, X.-N., Van Den Heuvel, M. P., Hagmann, P., Sporns, O., and Zatorre, R. J. (2018). Network-based asymmetry of the human auditory system. *Cerebral Cortex*, 28(7):2655–2664.

[102] Mišić, B., Betzel, R. F., Nematzadeh, A., Goni, J., Griffa, A., Hagmann, P., Flammini, A., Ahn, Y.-Y., and Sporns, O. (2015). Cooperative and competitive spreading dynamics on the human connectome. *Neuron*, 86(6):1518–1529.

[103] Murrough, J. W., Czermak, C., Henry, S., Nabulsi, N., Gallezot, J.-D., Gueorguieva, R., Planeta-Wilson, B., Krystal, J. H., Neumaier, J. F., Huang, Y., et al. (2011a). The effect of early trauma exposure on serotonin type 1b receptor expression revealed by reduced selective radioligand binding. *Archives of general psychiatry*, 68(9):892–900.

[104] Murrough, J. W., Henry, S., Hu, J., Gallezot, J.-D., Planeta-Wilson, B., Neumaier, J. F., and Neumeister, A. (2011b). Reduced ventral striatal/ventral pallidal sero-

tonin 1b receptor binding potential in major depressive disorder. *Psychopharmacology*, 213(2):547–553.

[105] Naganawa, M., Nabulsi, N., Henry, S., Matuskey, D., Lin, S.-F., Slieker, L., Schwarz, A. J., Kant, N., Jesudason, C., Ruley, K., et al. (2021). First-in-human assessment of 11c-lsn3172176, an m1 muscarinic acetylcholine receptor pet radiotracer. *Journal of Nuclear Medicine*, 62(4):553–560.

[106] Nelson, M. C., Royer, J., Leppert, I. R., Campbell, J. S., Schiavi, S., Jin, H., Tavakol, S., Vos de Wael, R., Rodriguez-Cruces, R., Pike, G. B., et al. (2023). The human brain connectome weighted by the myelin content and total intra-axonal cross-sectional area of white matter tracts. *bioRxiv*, pages 2023–03.

[107] Neumeister, A., Normandin, M. D., Murrough, J. W., Henry, S., Bailey, C. R., Luckenbaugh, D. A., Tuit, K., Zheng, M.-Q., Galatzer-Levy, I. R., Sinha, R., et al. (2012). Positron emission tomography shows elevated cannabinoid cb 1 receptor binding in men with alcohol dependence. *Alcoholism: Clinical and Experimental Research*, 36(12):2104–2109.

[108] Nørgaard, M., Beliveau, V., Ganz, M., Svarer, C., Pinborg, L. H., Keller, S. H., Jensen, P. S., Greve, D. N., and Knudsen, G. M. (2021). A high-resolution in vivo atlas of the human brain's benzodiazepine binding site of gabaa receptors. *NeuroImage*, 232:117878.

[109] Normandin, M. D., Zheng, M.-Q., Lin, K.-S., Mason, N. S., Lin, S.-F., Ropchan, J., Labaree, D., Henry, S., Williams, W. A., Carson, R. E., et al. (2015). Imaging the cannabinoid cb1 receptor in humans with [11c] omar: assessment of kinetic analysis methods, test–retest reproducibility, and gender differences. *Journal of Cerebral Blood Flow & Metabolism*, 35(8):1313–1322.

[110] Oldham, S., Fulcher, B. D., Aquino, K., Arnatkevičiūtė, A., Paquola, C., Shishegar, R., and Fornito, A. (2022). Modeling spatial, developmental, physiological, and topological constraints on human brain connectivity. *Science advances*, 8(22):eabm6127.

[111] Opel, N., Thalamuthu, A., Milaneschi, Y., Grotegerd, D., Flint, C., Leenings, R., Goltermann, J., Richter, M., Hahn, T., Woditsch, G., et al. (2020). Brain structural abnormalities in obesity: relation to age, genetic risk, and common psychiatric disorders. *Molecular psychiatry*, pages 1–14.

[112] Paquola, C., De Wael, R. V., Wagstyl, K., Bethlehem, R. A., Hong, S.-J., Seidlitz, J., Bullmore, E. T., Evans, A. C., Misic, B., Margulies, D. S., et al. (2019). Microstructural and functional gradients are increasingly dissociated in transmodal cortices. *PLoS biology*, 17(5):e3000284.

[113] Paquola, C., Royer, J., Lewis, L. B., Lepage, C., Glatard, T., Wagstyl, K., DeKraker, J., Toussaint, P.-J., Valk, S. L., Collins, L., et al. (2021). The bigbrainwarp toolbox for integration of bigbrain 3d histology with multimodal neuroimaging. *Elife*, 10:e70119.

[114] Paquola, C., Seidlitz, J., Benkarim, O., Royer, J., Klimes, P., Bethlehem, R. A., Larivière, S., Vos de Wael, R., Rodríguez-Cruces, R., Hall, J. A., et al. (2020). A multiscale cortical wiring space links cellular architecture and functional dynamics in the human brain. *PLoS biology*, 18(11):e3000979.

[115] Pittenger, C., Adams Jr, T. G., Gallezot, J.-D., Crowley, M. J., Nabulsi, N., Ropchan, J., Gao, H., Kichuk, S. A., Simpson, R., Billingslea, E., et al. (2016). Ocd is associated with an altered association between sensorimotor gating and cortical and subcortical 5-ht1b receptor binding. *Journal of affective disorders*, 196:87–96.

[116] Quackenbush, J. (2002). Microarray data normalization and transformation. *Nat Genet*, 32(4):496–501.

[117] Radhakrishnan, R., Matuskey, D., Nabulsi, N., Gaiser, E., Gallezot, J.-D., Henry, S., Planeta, B., Lin, S.-f., Ropchan, J., Huang, Y., et al. (2020). In vivo 5-ht6 and 5-ht2a receptor availability in antipsychotic treated schizophrenia patients vs. unmedicated healthy humans measured with [11c] gsk215083 pet. *Psychiatry Research: Neuroimaging*, 295:111007.

[118] Radhakrishnan, R., Nabulsi, N., Gaiser, E., Gallezot, J.-D., Henry, S., Planeta, B., Lin, S.-f., Ropchan, J., Williams, W., Morris, E., et al. (2018). Age-related change in 5-ht6 receptor availability in healthy male volunteers measured with 11c-gsk215083 pet. *Journal of Nuclear Medicine*, 59(9):1445–1450.

[119] Ranganathan, M., Cortes-Briones, J., Radhakrishnan, R., Thurnauer, H., Planeta, B., Skosnik, P., Gao, H., Labaree, D., Neumeister, A., Pittman, B., et al. (2016). Reduced brain cannabinoid receptor availability in schizophrenia. *Biological psychiatry*, 79(12):997–1005.

[120] Richiardi, J., Altmann, A., Milazzo, A.-C., Chang, C., Chakravarty, M. M., Banaschewski, T., Barker, G. J., Bokde, A. L., Bromberg, U., Büchel, C., et al. (2015). Correlated gene expression supports synchronous activity in brain networks. *Science*, 348(6240):1241–1244.

[121] Roberts, J. A., Perry, A., Lord, A. R., Roberts, G., Mitchell, P. B., Smith, R. E., Calamante, F., and Breakspear, M. (2016). The contribution of geometry to the human connectome. *Neuroimage*, 124:379–393.

[122] Romero-Garcia, R., Whitaker, K. J., Váša, F., Seidlitz, J., Shinn, M., Fonagy, P., Dolan, R. J., Jones, P. B., Goodyer, I. M., Bullmore, E. T., et al. (2018). Structural covariance networks are coupled to expression of genes enriched in supragranular layers of the human cortex. *NeuroImage*, 171:256–267.

[123] Salimi-Khorshidi, G., Douaud, G., Beckmann, C. F., Glasser, M. F., Griffanti, L., and Smith, S. M. (2014). Automatic denoising of functional mri data: combining independent component analysis and hierarchical fusion of classifiers. *Neuroimage*, 90:449–468.

[124] Sanchez-Rangel, E., Gallezot, J.-D., Yeckel, C. W., Lam, W., Belfort-DeAguiar, R., Chen, M.-K., Carson, R. E., Sherwin, R., and Hwang, J. J. (2020). Norepinephrine transporter availability in brown fat is reduced in obesity: a human pet study with [11 c] mrb. *International Journal of Obesity*, 44(4):964–967.

[125] Sandiego, C. M., Gallezot, J.-D., Lim, K., Ropchan, J., Lin, S.-f., Gao, H., Morris, E. D., and Cosgrove, K. P. (2015). Reference region modeling approaches for amphetamine challenge studies with [11c] flb 457 and pet. *Journal of Cerebral Blood Flow & Metabolism*, 35(4):623–629.

[126] Sandiego, C. M., Matuskey, D., Lavery, M., McGovern, E., Huang, Y., Nabulsi, N., Ropchan, J., Picciotto, M. R., Morris, E. D., McKee, S. A., et al. (2018). The effect of treatment with guanfacine, an alpha2 adrenergic agonist, on dopaminergic tone in tobacco smokers: An [11 c] flb457 pet study. *Neuropsychopharmacology*, 43(5):1052–1058.

[127] Saricicek, A., Chen, J., Planeta, B., Ruf, B., Subramanyam, K., Maloney, K., Matuskey, D., Labaree, D.,

Deserno, L., Neumeister, A., et al. (2015). Test–retest reliability of the novel 5-ht 1b receptor pet radioligand [11 c] p943. *European journal of nuclear medicine and molecular imaging*, 42(3):468–477.

[128] Savli, M., Bauer, A., Mitterhauser, M., Ding, Y.-S., Hahn, A., Kroll, T., Neumeister, A., Haeusler, D., Ungersboeck, J., Henry, S., et al. (2012). Normative database of the serotonergic system in healthy subjects using multi-tracer pet. *Neuroimage*, 63(1):447–459.

[129] Schaefer, A., Kong, R., Gordon, E. M., Laumann, T. O., Zuo, X.-N., Holmes, A. J., Eickhoff, S. B., and Yeo, B. T. (2018). Local-global parcellation of the human cerebral cortex from intrinsic functional connectivity mri. *Cerebral cortex*, 28(9):3095–3114.

[130] Schmaal, L., Hibar, D., Sämann, P. G., Hall, G., Baune, B., Jahanshad, N., Cheung, J., Van Erp, T., Bos, D., Ikram, M. A., et al. (2017). Cortical abnormalities in adults and adolescents with major depression based on brain scans from 20 cohorts worldwide in the enigma major depressive disorder working group. *Molecular psychiatry*, 22(6):900–909.

[131] Sebenius, I., Seidlitz, J., Warrier, V., Bethlehem, R. A., Alexander-Bloch, A., Mallard, T., Garcia, R. R., Bullmore, E. T., and Morgan, S. E. (2022). Mind networks: Robust estimation of structural similarity from brain mri. *bioRxiv*.

[132] Seeley, W. W., Crawford, R. K., Zhou, J., Miller, B. L., and Greicius, M. D. (2009). Neurodegenerative diseases target large-scale human brain networks. *Neuron*, 62(1):42–52.

[133] Seguin, C., Tian, Y., and Zalesky, A. (2020). Network communication models improve the behavioral and functional predictive utility of the human structural connectome. *Network Neuroscience*, 4(4):980–1006.

[134] Seidlitz, J., Váša, F., Shinn, M., Romero-Garcia, R., Whitaker, K. J., Vértes, P. E., Wagstyl, K., Reardon, P. K., Clasen, L., Liu, S., et al. (2018). Morphometric similarity networks detect microscale cortical organization and predict inter-individual cognitive variation. *Neuron*, 97(1):231–247.

[135] Shafiei, G., Baillet, S., and Misic, B. (2022a). Human electromagnetic and haemodynamic networks systematically converge in unimodal cortex and diverge in transmodal cortex. *PLoS biology*, 20(8):e3001735.

[136] Shafiei, G., Bazinet, V., Dadar, M., Manera, A. L., Collins, D. L., Dagher, A., Borroni, B., Sanchez-Valle, R., Moreno, F., Laforce, R., et al. (2022b). Network structure and transcriptomic vulnerability shape atrophy in frontotemporal dementia. *Brain*.

[137] Shafiei, G., Markello, R. D., De Wael, R. V., Bernhardt, B. C., Fulcher, B. D., and Misic, B. (2020a). Topographic gradients of intrinsic dynamics across neocortex. *Elife*, 9:e62116.

[138] Shafiei, G., Markello, R. D., Makowski, C., Talpalaru, A., Kirschner, M., Devenyi, G. A., Guma, E., Hagmann, P., Cashman, N. R., Lepage, M., et al. (2020b). Spatial patterning of tissue volume loss in schizophrenia reflects brain network architecture. *Biological psychiatry*, 87(8):727–735.

[139] Slifstein, M., Van De Giessen, E., Van Snellenberg, J., Thompson, J. L., Narendran, R., Gil, R., Hackett, E., Girgis, R., Ojeil, N., Moore, H., et al. (2015). Deficits in prefrontal cortical and extrastriatal dopamine release in schizophrenia: a positron emission tomographic func-

tional magnetic resonance imaging study. *JAMA psychiatry*, 72(4):316–324.

[140] Smart, K., Cox, S. M., Scala, S. G., Tippler, M., Jaworska, N., Boivin, M., Séguin, J. R., Benkelfat, C., and Leyton, M. (2019). Sex differences in [11 c] abp688 binding: a positron emission tomography study of mglu5 receptors. *European journal of nuclear medicine and molecular imaging*, 46(5):1179–1183.

[141] Smith, C. T., Crawford, J. L., Dang, L. C., Seaman, K. L., San Juan, M. D., Vijay, A., Katz, D. T., Matuskey, D., Cowan, R. L., Morris, E. D., et al. (2019). Partial-volume correction increases estimated dopamine d2-like receptor binding potential and reduces adult age differences. *Journal of Cerebral Blood Flow & Metabolism*, 39(5):822–833.

[142] Smith, R. E., Tournier, J.-D., Calamante, F., and Connelly, A. (2015). Sift2: Enabling dense quantitative assessment of brain white matter connectivity using streamlines tractography. *Neuroimage*, 119:338–351.

[143] Sporns, O. and Betzel, R. F. (2016). Modular brain networks. *Annual review of psychology*, 67:613–640.

[144] Sporns, O., Honey, C. J., and Kötter, R. (2007). Identification and classification of hubs in brain networks. *PloS one*, 2(10):e1049.

[145] Sporns, O., Tononi, G., and Kötter, R. (2005). The human connectome: a structural description of the human brain. *PLoS computational biology*, 1(4):e42.

[146] Stiso, J. and Bassett, D. S. (2018). Spatial embedding imposes constraints on neuronal network architectures. *Trends in cognitive sciences*, 22(12):1127–1142.

[147] Suárez, L. E., Markello, R. D., Betzel, R. F., and Misic, B. (2020). Linking structure and function in macroscale brain networks. *Trends Cogn Sci*.

[148] Sun, D., Ching, C. R., Lin, A., Forsyth, J. K., Kushan, L., Vajdi, A., Jalbrzikowski, M., Hansen, L., Villalon-Reina, J. E., Qu, X., et al. (2020). Large-scale mapping of cortical alterations in 22q11. 2 deletion syndrome: convergence with idiopathic psychosis and effects of deletion size. *Molecular psychiatry*, 25(8):1822–1834.

[149] Sydnor, V. J., Larsen, B., Bassett, D. S., Alexander-Bloch, A., Fair, D. A., Liston, C., Mackey, A. P., Milham, M. P., Pines, A., Roalf, D. R., et al. (2021). Neurodevelopment of the association cortices: Patterns, mechanisms, and implications for psychopathology. *Neuron*, 109(18):2820–2846.

[150] Tadel, F., Baillet, S., Mosher, J. C., Pantazis, D., and Leahy, R. M. (2011). Brainstorm: a user-friendly application for meg/eeg analysis. *Computational intelligence and neuroscience*, 2011.

[151] Thompson, P. M., Jahanshad, N., Ching, C. R., Salminen, L. E., Thomopoulos, S. I., Bright, J., Baune, B. T., Bertolín, S., Bralten, J., Bruin, W. B., et al. (2020). Enigma and global neuroscience: A decade of large-scale studies of the brain in health and disease across more than 40 countries. *Translational psychiatry*, 10(1):1–28.

[152] Tournier, J. D., Calamante, F., Connelly, A., et al. (2010). Improved probabilistic streamlines tractography by 2nd order integration over fibre orientation distributions. In *Proceedings of the international society for magnetic resonance in medicine*, volume 1670. John Wiley & Sons, Inc. New Jersey, USA.

[153] Tournier, J.-D., Smith, R., Raffelt, D., Tabbara, R., Dhollander, T., Pietsch, M., Christiaens, D., Jeurissen, B., Yeh, C.-H., and Connelly, A. (2019). Mrtrix3: A fast, flexible

and open software framework for medical image processing and visualisation. *Neuroimage*, 202:116137.

[154] Uddin, L. Q., Mooshagian, E., Zaidel, E., Scheres, A., Margulies, D. S., Kelly, A. C., Shehzad, Z., Adelstein, J. S., Castellanos, F. X., Biswal, B. B., et al. (2008). Residual functional connectivity in the split-brain revealed with resting-state fmri. *Neuroreport*, 19(7):703.

[155] Vaishnavi, S. N., Vlassenko, A. G., Rundle, M. M., Snyder, A. Z., Mintun, M. A., and Raichle, M. E. (2010). Regional aerobic glycolysis in the human brain. *Proceedings of the National Academy of Sciences*, 107(41):17757–17762.

[156] Van Den Heuvel, M. P., Mandl, R. C., Kahn, R. S., and Hulshoff Pol, H. E. (2009). Functionally linked resting-state networks reflect the underlying structural connectivity architecture of the human brain. *Human brain mapping*, 30(10):3127–3141.

[157] Van Den Heuvel, M. P. and Sporns, O. (2011). Rich-club organization of the human connectome. *Journal of Neuroscience*, 31(44):15775–15786.

[158] Van den Heuvel, M. P. and Sporns, O. (2013). Network hubs in the human brain. *Trends in cognitive sciences*, 17(12):683–696.

[159] Van Erp, T. G., Walton, E., Hibar, D. P., Schmaal, L., Jiang, W., Glahn, D. C., Pearlson, G. D., Yao, N., Fukunaga, M., Hashimoto, R., et al. (2018). Cortical brain abnormalities in 4474 individuals with schizophrenia and 5098 control subjects via the enhancing neuro imaging genetics through meta analysis (enigma) consortium. *Biological psychiatry*, 84(9):644–654.

[160] Van Essen, D. C., Smith, S. M., Barch, D. M., Behrens, T. E., Yacoub, E., Ugurbil, K., Consortium, W.-M. H., et al. (2013). The wu-minn human connectome project: an overview. *Neuroimage*, 80:62–79.

[161] Van Rooij, D., Anagnostou, E., Arango, C., Auzias, G., Behrmann, M., Busatto, G. F., Calderoni, S., Daly, E., Deruelle, C., Di Martino, A., et al. (2018). Cortical and subcortical brain morphometry differences between patients with autism spectrum disorder and healthy individuals across the lifespan: results from the enigma asd working group. *American Journal of Psychiatry*, 175(4):359–369.

[162] Vasa, F. and Misic, B. (2022). Null models in network neuroscience. *Nat Rev Neurosci*.

[163] Vázquez-Rodríguez, B., Suárez, L. E., Markello, R. D., Shafiei, G., Paquola, C., Hagmann, P., Van Den Heuvel, M. P., Bernhardt, B. C., Spreng, R. N., and Misic, B. (2019). Gradients of structure–function tethering across neocortex. *Proceedings of the National Academy of Sciences*, 116(42):21219–21227.

[164] Vértes, P., Rittman, T., Whitaker, K., Romero-Garcia, R., Váša, F., Kitzbichler, M., Fonagy, P., Dolan, R., Jones, P., Goodyer, I., et al. (2016). Gene transcription profiles associated with intra-modular and inter-modular hubs in human fmri networks. *Philos Trans R Soc Lond B Biol Sci*, 371:735–769.

[165] Voigt, K., Liang, E. X., Misic, B., Ward, P. G. D., Egan, G. F., and Jamadar, S. D. (2022). Metabolic and functional connectivity provide unique and complementary insights into cognition-connectome relationships. *Cerebral Cortex*.

[166] von Economo, C. F. and Koskinas, G. N. (1925). *Die cytoarchitektonik der hirnrinde des erwachsenen menschen*. J. Springer.

[167] Voytek, B. (2022). The data science future of neuroscience theory. *Nature Methods*, pages 1–2.

[168] Wang, B., Mezlini, A. M., Demir, F., Fiume, M., Tu, Z., Brudno, M., Haibe-Kains, B., and Goldenberg, A. (2014). Similarity network fusion for aggregating data types on a genomic scale. *Nature methods*, 11(3):333–337.

[169] Warren, J. D., Rohrer, J. D., Schott, J. M., Fox, N. C., Hardy, J., and Rossor, M. N. (2013). Molecular nexopathies: a new paradigm of neurodegenerative disease. *Trends in neurosciences*, 36(10):561–569.

[170] Whelan, C. D., Altmann, A., Botía, J. A., Jahanshad, N., Hibar, D. P., Absil, J., Alhusaini, S., Alvim, M. K., Auvinen, P., Bartolini, E., et al. (2018). Structural brain abnormalities in the common epilepsies assessed in a worldwide enigma study. *Brain*, 141(2):391–408.

[171] Xu, T., Nenning, K.-H., Schwartz, E., Hong, S.-J., Vogelstein, J. T., Goulas, A., Fair, D. A., Schroeder, C. E., Margulies, D. S., Smallwood, J., et al. (2020). Cross-species functional alignment reveals evolutionary hierarchy within the connectome. *Neuroimage*, 223:117346.

[172] Yeo, B., Krienen, F. M., Sepulcre, J., Sabuncu, M. R., Lashkari, D., Hollinshead, M., Roffman, J. L., Smoller, J. W., Zöllei, L., Polimeni, J. R., et al. (2011). The organization of the human cerebral cortex estimated by intrinsic functional connectivity. *J Neurophysiol*, 106(3):1125–1165.

[173] Zakiniaeiz, Y., Hillmer, A. T., Matuskey, D., Nabulsi, N., Ropchan, J., Mazure, C. M., Picciotto, M. R., Huang, Y., McKee, S. A., Morris, E. D., et al. (2019). Sex differences in amphetamine-induced dopamine release in the dorsolateral prefrontal cortex of tobacco smokers. *Neuropsychopharmacology*, 44(13):2205–2211.

[174] Zalesky, A., Fornito, A., Cocchi, L., Gollo, L. L., van den Heuvel, M. P., and Breakspear, M. (2016). Connectome sensitivity or specificity: which is more important? *Neuroimage*, 142:407–420.

[175] Zheng, Y.-Q., Zhang, Y., Yau, Y., Zeighami, Y., Larcher, K., Misic, B., and Dagher, A. (2019). Local vulnerability and global connectivity jointly shape neurodegenerative disease propagation. *PLoS Biol*, 17(11).
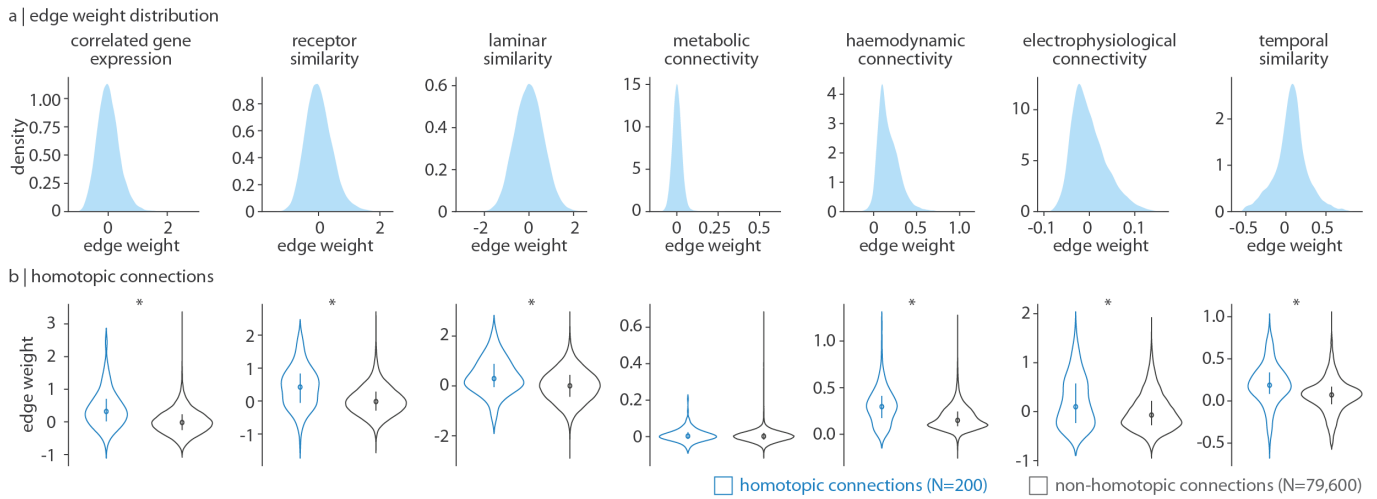
Figure S1. **Distributions of normalized edge weight for each connectivity mode |** (a) Edge weight distributions of each normalized connectivity mode. (b) Edge weight distributions for homotopic ($N = 200$ edges; blue) and non-homotopic ($N = 79\,600$; grey) edges. Significance was determined using two-tailed Welch's t-test.
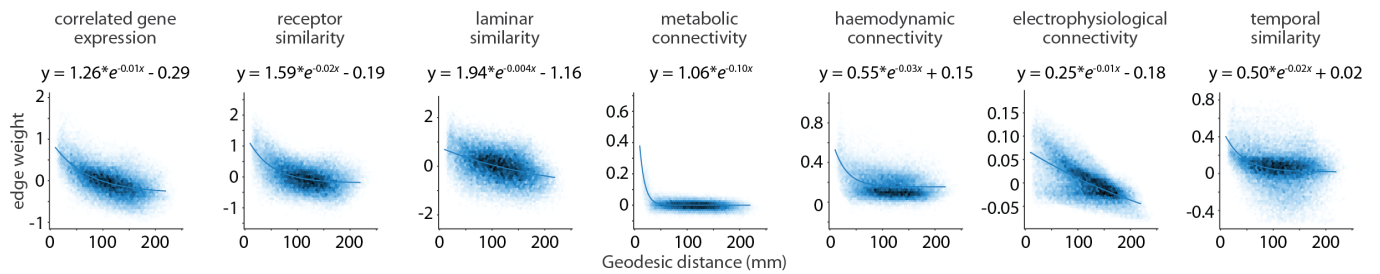

Figure S2. **Relationship between edge strength and geodesic distance |** Edge weights between pairs of brain regions within the same hemisphere decrease with geodesic distance across all seven connectivity modes. Darker colours represent a greater density of points. This relationship is better fit with an exponential rather than linear function (exponential equations shown on top). Note that geodesic distance—the distance along the surface of the brain between two regions—is only computed within hemispheres so between-hemisphere edges are excluded from the analysis.
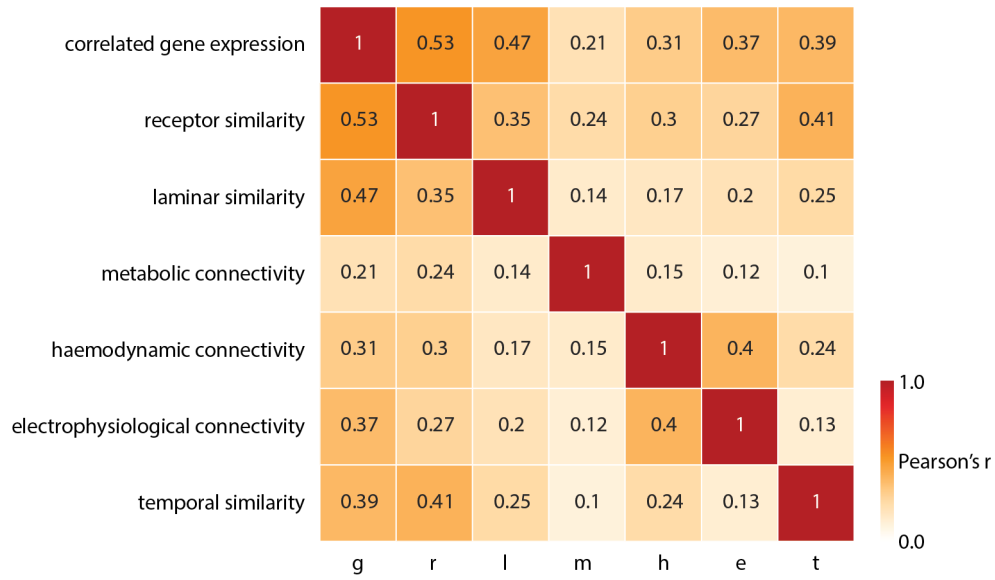
Figure S3. **Edge-wise correspondence between connectivity modes |** Pearson's correlation of the upper triangle of every pair of connectivity modes included in the analyses.
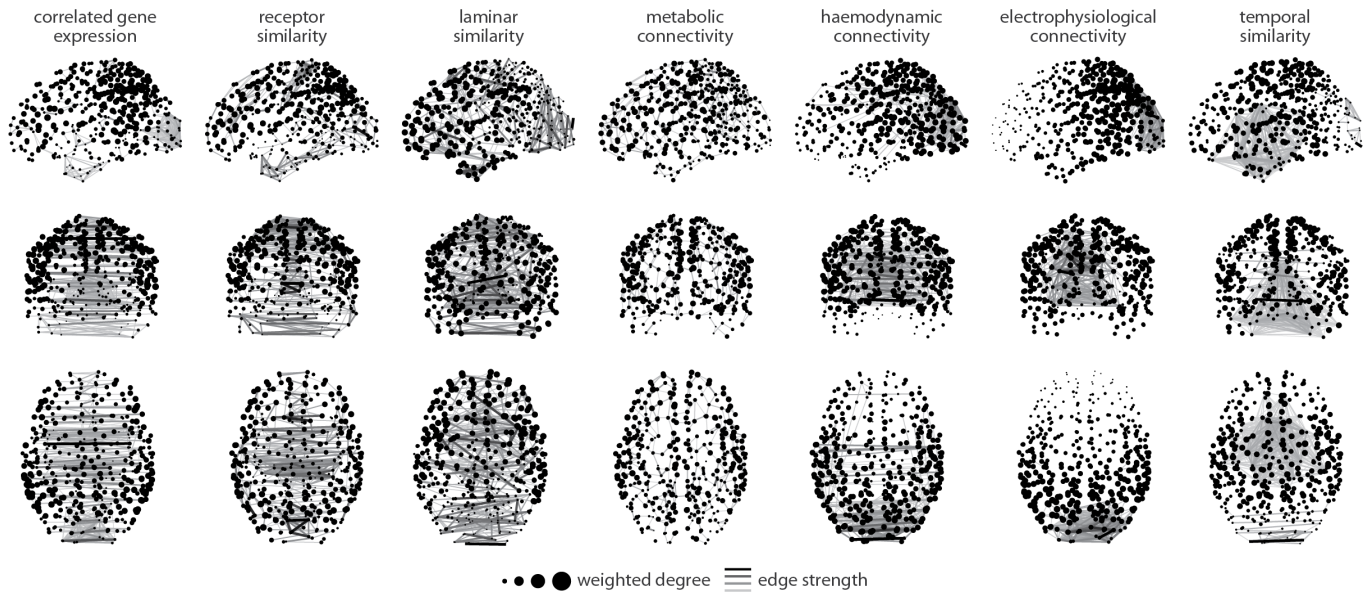

Figure S4. **Alternative views of the strongest edges in each connectivity mode |** For each connectivity mode, we plot the 0.5% strongest edges. Darker and thicker lines indicate stronger edges. Points represent brain regions and are sized according to the sum of edge weights (weighted degree). Here we show sagittal, coronal, and axial views to complement Fig. 3a.
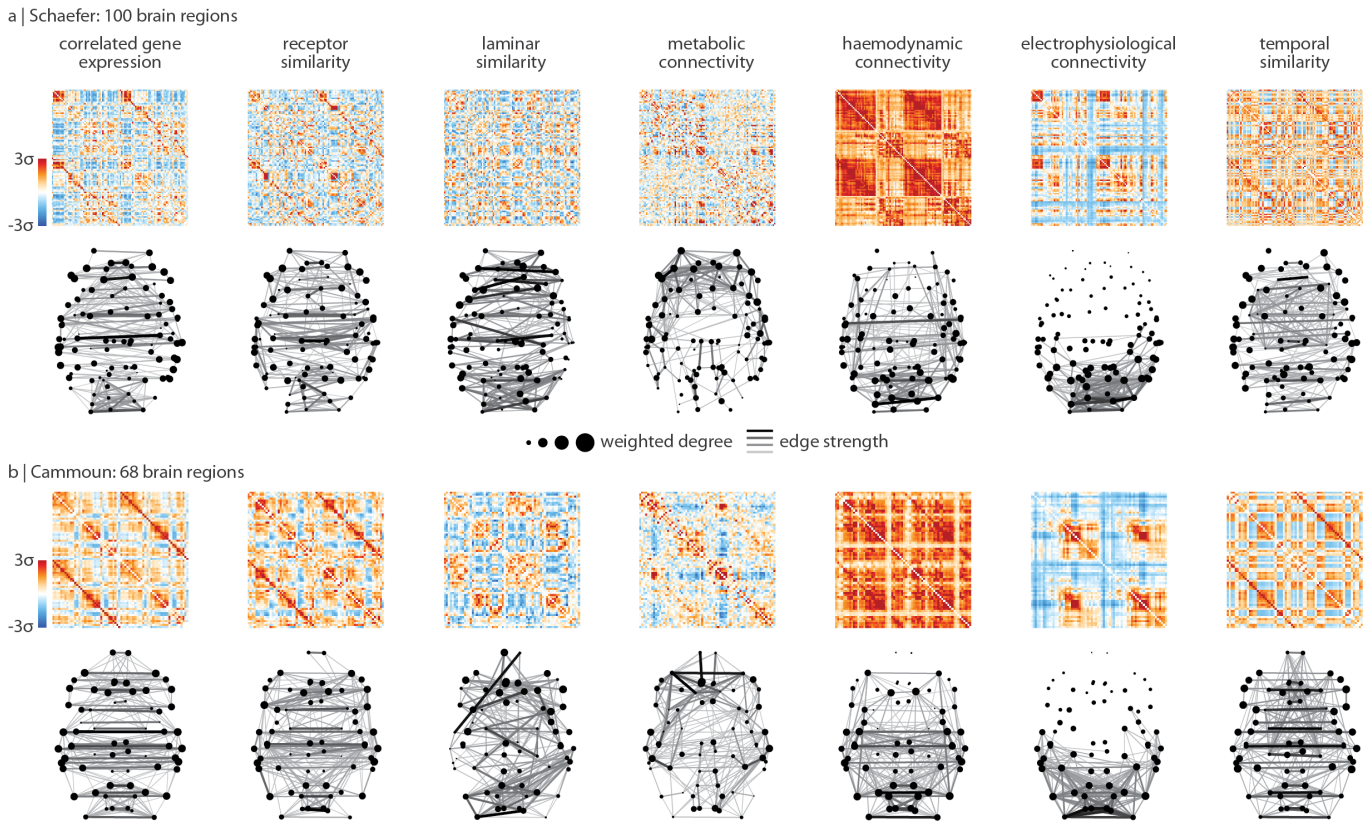
a | Schaefer: 100 brain regions

Figure S5. **Replication using alternative parcellations |** Analyses were repeated using (a) the 100-region Schaefer parcellation and (b) the 68-region Cammoun parcellation (regionally equivalent to the Desikan-Killiany atlas) [30, 39, 129]. We show each network as well as the the 5% (for Schaefer) or 10% (for Cammoun) strongest edges of the network.
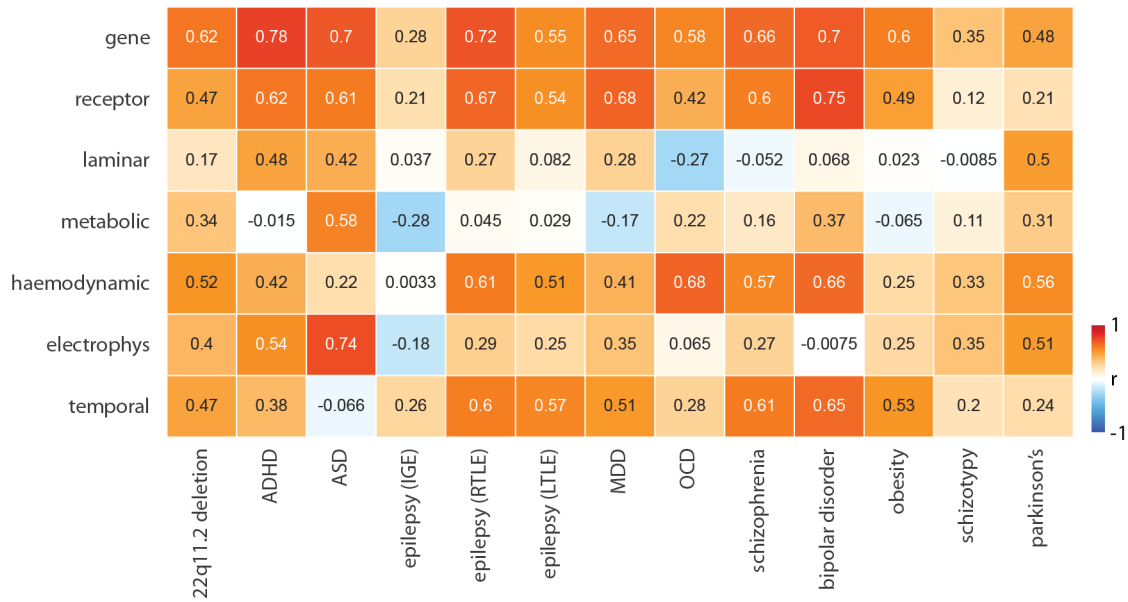

Figure S6. **Contributions of connectivity modes to disease vulnerability |** We repeat the procedure in Fig. 4 after regressing the exponential relationship with Euclidean distance (shown in Fig. 1b) from each connectivity mode.
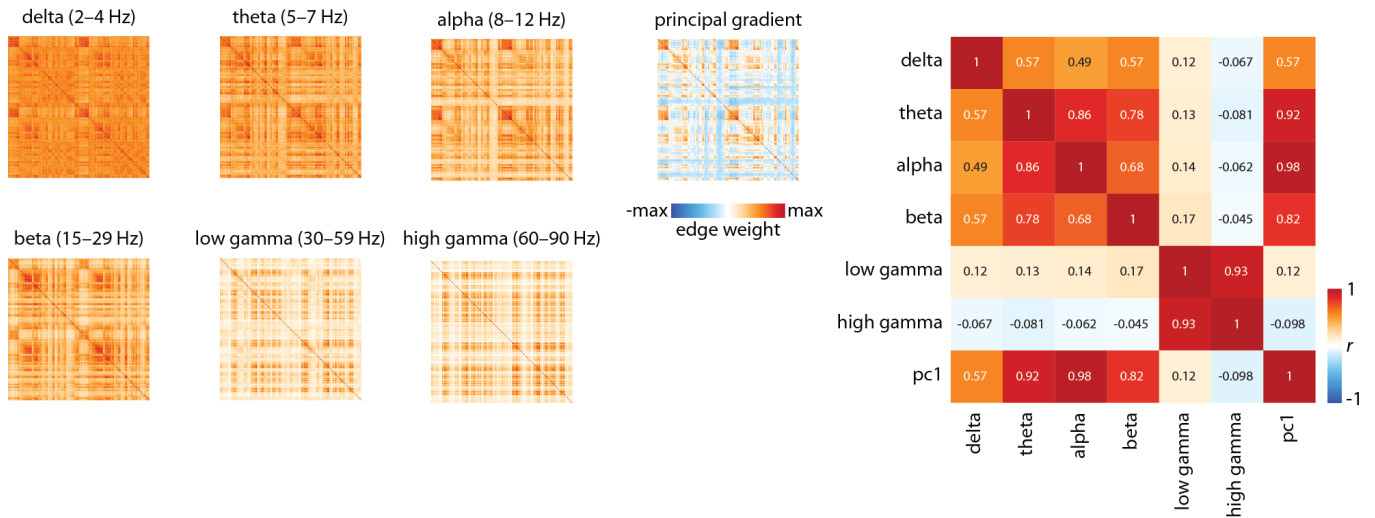
Figure S7. **MEG connectomes across frequency bands |** Amplitude envelope correlations were performed between time-series at each pair of brain regions for six canonical frequency bands separately (delta (2–4 Hz), theta (5–7 Hz), alpha (8–12 Hz), beta (15–29 Hz), low gamma (30–59 Hz), high gamma (60–90 Hz). The electrophysiological connectivity mode used in the present analyses is the first principal component of the vectorized upper triangles of all six frequency-dependent connectivity matrices. On the right we show Pearson's correlations between the six frequency-dependent connectivity matrices and the principal gradient, showing that the first gradient is a good proxy for electrophysiological connectivity.

Receptor/ transporter	Neurotransmitter	Tracer	Measure	N	References
D_1	dopamine	$[^{11}C]$SCH23390	BP_{ND}	13 (7)	[79]
D_2	dopamine	$[^{11}C]$FLB-457	BP_{ND}	92 (49)	[125, 126, 139, 141, 173]
DAT	dopamine	$[^{123}I]$-FP-CIT	SUVR	174 (65)	[44]
NET	norepinephrine	$[^{11}C]$MRB	BP_{ND}	77 (27)	[18, 31, 41, 124]
5-HT$_{1A}$	serotonin	$[^{11}C]$WAY-100635	BP_{ND}	35 (17)	[128]
5-HT$_{1B}$	serotonin	$[^{11}C]$P943	BP_{ND}	88 (24)	[10, 53, 99, 103, 104, 115, 127, 128]
5-HT$_{2A}$	serotonin	$[^{11}C]$Cimbi-36	B_{max}	29 (14)	[19]
5-HT$_4$	serotonin	$[^{11}C]$SB207145	B_{max}	59 (18)	[19]
5-HT$_6$	serotonin	$[^{11}C]$GSK215083	BP_{ND}	30 (0)	[117, 118]
5-HTT	serotonin	$[^{11}C]$DASB	B_{max}	100 (71)	[19]
$\alpha_4\beta_2$	acetylcholine	$[^{18}F]$flubatine	V_T	30 (10)	[9, 69]
M_1	acetylcholine	$[^{11}C]$LSN3172176	BP_{ND}	24 (11)	[105]
VAChT	acetylcholine	$[^{18}F]$FEOBV	SUVR	30 (18)	[2, 17, 60]
mGluR$_5$	glutamate	$[^{11}C]$ABP688	BP_{ND}	123 (71)	[43, 60, 140]
GABA$_{A/BZ}$	GABA	$[^{11}C]$flumazenil	B_{max}	16 (9)	[108]
H$_3$	histamine	$[^{11}C]$GSK189254	V_T	8 (1)	[54]
CB$_1$	cannabinoid	$[^{11}C]$OMAR	V_T	77 (28)	[45, 107, 109, 119]
MOR	opioid	$[^{11}C]$carfentanil	BP_{ND}	204 (72)	[80]

TABLE S1. **Neurotransmitter receptors and transporters included in receptor similarity |** BP_{ND} = non-displaceable binding potential; V_T = tracer distribution volume; B_{max} = density (pmol/ml) converted from binding potential (5-HT) or distributional volume (GABA) using autoradiography-derived densities; SUVR = standard uptake value ratio. Values in parentheses (under N) indicate number of females. This table is adapted from Table 1 of [60].